이학석사 학위논문

Study on the microstructures and seismic anisotropy of blueschist and eclogite from Ring Mountain and Jenner in California

캘리포니아의 링 마운틴과 제너에서 산출되는 청색편암과 에클로자이트의 미구조와 지진파 비등방성 연구

2016 년 2 월

서울대학교 대학원

지구환경과학부

하 윤 해

Abstract

Study on the microstructures and seismic anisotropy of blueschist and eclogite from Ring Mountain and Jenner in California

Yoonhae Ha
School of Earth and Environment Sciences
The Graduate school
Seoul National University

Seismic anisotropy has been observed in many subduction zones. During subduction of slab, the oceanic crust changes to blueschist and eclogite. Since minerals in blueschist are very anisotropic elastically, seismic properties in the subducting slab can be attributed to the lattice preferred orientation (LPO) of these minerals. We studied microstructures and seismic properties of blueschist and eclogite from Ring Mt. and Jenner in California. Blueschist samples are mainly composed of glaucophane, epidote and phengite. Eclogite samples are mostly composed of omphacite, glaucophane, epidote and garnet. We determined LPOs of minerals using SEM/EBSD and calculated seismic properties of minerals and whole rocks.

LPOs of glaucophane showed [001] axes are aligned subparallel to lineation, and both (110) poles and [100] axes subnormal to foliation. Glaucophane in samples from Jenner, however, exhibited [001] axes forming a girdle subparallel to lineation. Seismic anisotropy of glaucophane was stronger in samples from Ring Mt. than those from Jenner. Epidote showed

[001] axes are aligned subnormal to foliation and (110) and (010) poles subparallel to lineation. LPOs of phengite were characterized by a maximum of [001] axes normal to foliation, with (110) and (010) poles and [100] axes aligning in a girdle parallel to foliation. Phengite showed the strongest seismic anisotropy among major minerals. LPOs of omphacite showed that [010] axes subnormal to foliation and [001] axes are aligned subparallel to lineation and foliation with a girdle in eclogites and blueschist, respectively. Seismic anisotropy of omphacite was very weak. Blueschist from Ring Mt. showed stronger seismic anisotropy than those from Jenner because samples from Jenner included high contents of garnet ± omphacite. Especially, blueschist including abundant phengite showed very strong seismic anisotropy (AV_P = 30%, max.AV_S = 23%). Eclogite showed much weaker seismic anisotropy (AV_P = 5-6%, max.AV_S = 4-6%) than blueschist (AV_P = 12-30%, max.AV_S = 9-23%). Therefore, strong seismic anisotropy observed in subduction zone can be more affected by blueschist than eclogite.

Keywords: blueschist, eclogite, phengite, lattice preferred orientation, seismic anisotropy, Franciscan complex

Student Number: 2014-20322

Contents

Chapter 1. Introduction

In many subduction zones, strong seismic anisotropy has been observed (e.g., Fouch and Fischer, 1996; Currie et al., 2004; Long and van der Hilst, 2005; Pozgay et al., 2007). Agostinetti and Miller (2014) suggested it would be associated with metamorphism in the subducting oceanic plate and dehydration process in the mantle. During subduction, the oceanic crust changes to diverse metamorphic facies such as blueschist according to P-T conditions resulting in eclogite facies (Hacker et al., 2003). Blueschist is a metamorphic facies rock existing at high pressure and low temperature conditions in subducting oceanic crust and forms the major proportion of the top of slab. The transformation blueschist-to-eclogite is a common process during subduction and blueschist overprinting is occurred during exhumation. Blueschist is dominated by hydrous minerals such as glaucophane, lawsonite, epidote, and chlorite. Since these minerals are very anisotropic elastically (Schmidt and Poli, 1998; Mao et al., 2007; Bezacier et al., 2010), seismic velocity and anisotropy in subduction zone can be attributed to the lattice preferred orientations (LPO) of these minerals. Therefore, investigations of microstructures of blueschist are important to understand seismic velocity and anisotropy of the subducting oceanic crust.

A few previous studies have been conducted about deformation microstructures and seismic properties of the deformed natural blueschist

(Bezacier et al., 2010; Fujimoto et al., 2010; Teyssier et al., 2010; Cao et al., 2011; Cao et al., 2013; Kim et al., 2013a, 2013b; Cao et al., 2014). Based on these studies, they showed that the major forming minerals of blueschist (glaucophane, lawsonite, and epidote) have strong LPOs. They showed slip systems of glaucophane are (100)[001] and {110}[001], and slip systems of epidote were (001)[010] and {101}[010]. Seismic anisotropy of blueschist (AV_P > 10%) is generally stronger than that of eclogite (AV_P < 3%) and surrounding mantle rocks (Bascou et al., 2001; Fujimoto et al., 2010). On the other hand, eclogite (V_P = 8.0–8.6 km/s) shows significantly higher seismic velocities than blueschist (V_P = 7.3–7.6 km/s) (Rudnick and Fountain, 1995; Fujimoto et al., 2010).

Phengite is magnesium-bearing muscovite, and can develop very strong LPO when it is deformed. Besides, seismic anisotropy of muscovite single crystal is very strong (AV_P = 44.2%, AV_S = 50.7%) (Ji et al., 2002). In this study, we present the deformation microstructures and seismic properties of the naturally deformed epidote-blueschists with high content of phengite and eclogites collected from Ring Mountain and Jenner Headlands of the Franciscan Complex, Western California.

Chapter 2. Geological background

The Franciscan Complex of the California Coast Ranges is the classic accretionary prism (Figure 1). It was formed during the eastward dipping subduction of the Farallon plate beneath the North American plate from Late-Jurassic thorough Tertiary (Hamilton, 1969; Bailey et al., 1970; Ernst, 1970; Berkland et al., 1972; Blake et al., 1988). However, most exposed rocks are accreted between ca.120 and 32 Ma (e.g. Blake et al., 1988; Wakabayashi, 1992; Wakabayashi and Dumitru, 2007; Ernst, 2011). About a fourth of them are blueschist formed under the high pressure and low temperature conditions or higher grade metamorphic rocks. High grade rocks, however, developed the initiation of subduction during 165-135 Ma, that is the oldest metamorphic rocks in the Franciscan (Ross and Sharp, 1986, 1988; Anczkiewicz et al., 2004; Wakabayashi and Dumitru, 2007; Shervais et al., 2011). Many Franciscan metamorphic rocks lack a post-subduction thermal overprint suggesting exhumation to near the surface prior to subduction termination (Ernst, 1988). The Franciscan Complex is divided into three northwest trending belts by lithologic character, age, and degree of deformation; the Coastal (Western) Belt, the Central (mélange) Belt, and the Eastern Belt (Bailey et al., 1964; Ernst, 1970). Metamorphic temperature and age increase from west to east. The sample location in this study, Ring Mountain and Jenner, are both located in Central Belt. The detailed geology maps of both

areas and sample localities are shown in Figure 2A (Ring Mountain) and 2B (Jenner). The Central Belt is characterized as a serpentinite or mud-matrix mélange containing isolated blocks originated from both down-going and overriding plates (Bailey et al., 1964; Ernst, 1970; Cloos, 1983, 1986; Blake et al., 1988; Shervais et al., 2011). High-pressure and low-temperature metamorphic rocks of blueschist, eclogite, and amphibolite are found chiefly as this isolated small blocks (Cloos, 1986). These blocks are called “high-grade blocks” meaning mafic blocks metamorphosed at high pressure and concentrated in the Central belt (Coleman and Lanphere, 1971). P-T conditions of them inferred to counterclockwise P-T path (Oh and Liou, 1990; Wakabayashi, 1990; Krogh et al., 1994) suggest that prograde eclogitization of a subducting slab and later exhumation and blueschist facies overprinting by decreasing geothermal gradient (Tsujimori et al., 2006). The exhumation of high-grade blocks occurred in a serpentinite matrix (Wakabayashi, 2015) and the rinds which are composed of actinolite, chlorite are formed by chemical reaction between the blocks and serpentinite during retrograde process (Coleman and Lanphere, 1971). However, overprinting of lower−grade blueschist developed along the margin of blocks. Pseudomorphs of high pressure minerals and preservation of cavities suggest alterations caused by retrograde process and transport to crustal levels occurred without penetrative deformation of the interior of many blocks (Cloos, 1986). High-grade blueschist and eclogite samples in this study, therefore, show prograde subduction deformation structures.

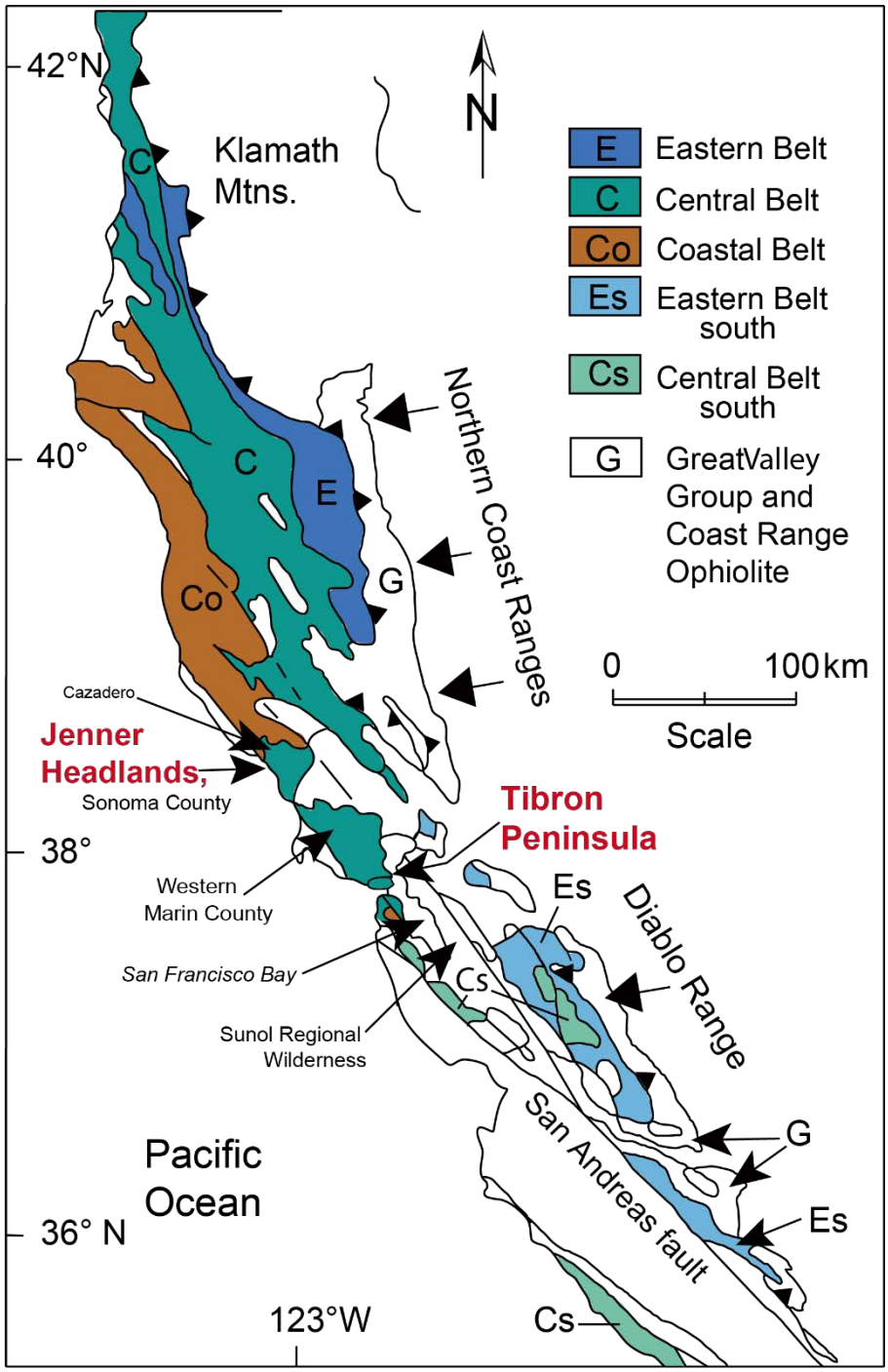

Figure 1. Generalized geologic map of western California, showing distribution of large areas of the three traditional belts of the Franciscan complex. Modified from Raymond and Bero, 2015.

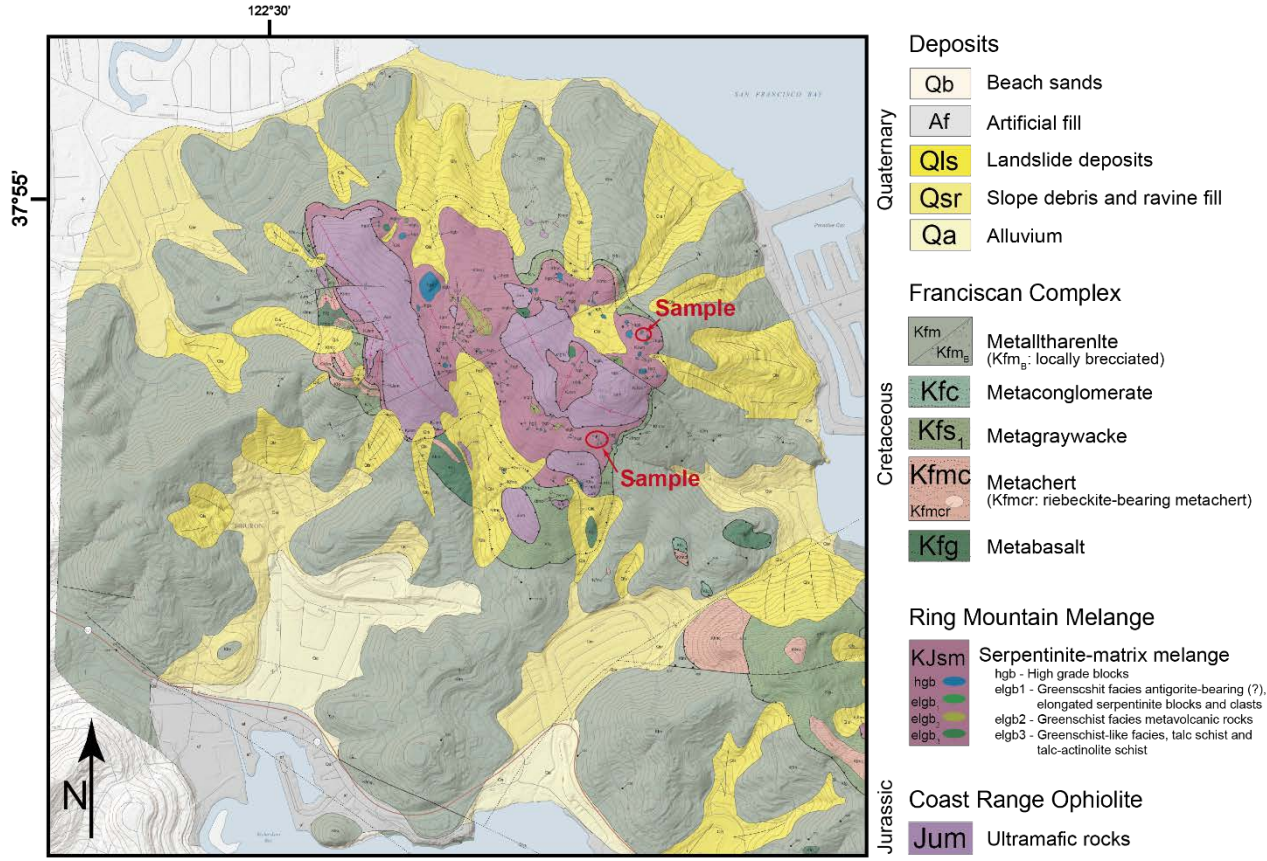

Figure 2A. Detailed geologic map of Ring Mountain. The sample locations are marked as red arrows. Modified from Bero (2014)

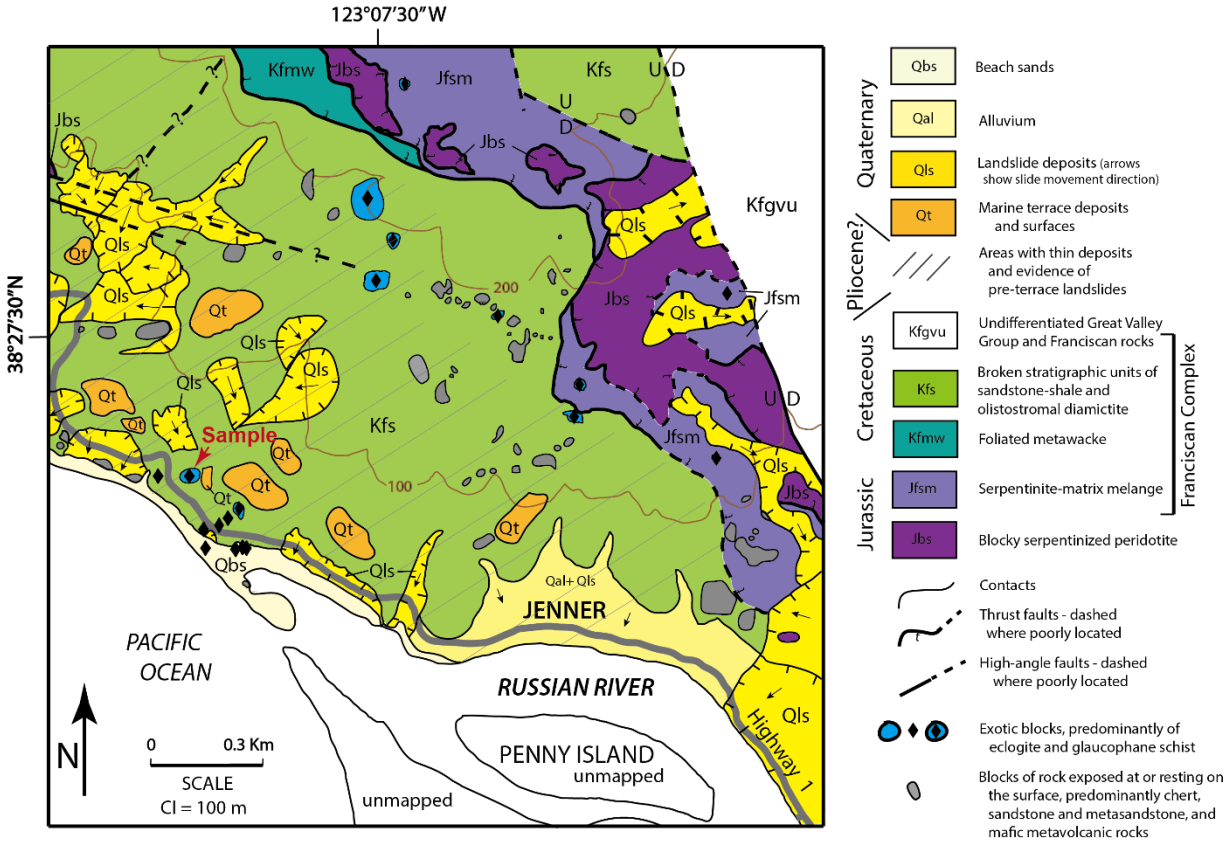

Figure 2B. Detailed geologic map of Jenner (Raymond, 2015). The sample locations are marked as red arrows.

Chapter 3. Sample description

We selected five samples from Ring Mountain (2100, 2097, 2099-1, 2425, and 2099-2) and four samples from Jenner Headlands (2091, 2089, 2090, and 2088). The modal compositions of samples are shown in Table 1. Two samples from each locations are eclogites which are mostly composed of omphacite, epidote, glaucophane and garnet. A sample from Ring Mountain (2099-2) show a mineral assemblage of omphacite (51%) + epidote (33%) + glaucophane (8%) + garnet (5%) + sphene (3%). The other eclogite sample from Jenner (2088) includes very high content of glaucophane (amphibole) showing a mineral assemblage of glaucophane (40%) + omphacite (25%) + sphene (12%) + garnet (8%) + phengite (7%) with minor chlorite and epidote. Most blueschist samples are epidote-blueschist close to eclogite. They show compositional layering of eclogite and blueschist facies in mm to cm scale. Coleman et al. (1965) interpreted that the interlayered high grade blocks may have been formed contemporaneously. The sample 2099 collected from Ring Mountain shows relatively thicker alternative layering, therefore, we subdivided into blueschist (2099-1) and eclogite parts (2099-2). Epidote-blueschist are relatively coarse grained and strongly deformed. Epidote-blueschist show a mineral assemblage of glaucophane (37–58%) + epidote (1–49%) + phengite (0–40%) + sphene (0–15%) ± (chlorite, omphacite,

garnet). Some blueschist samples show very high content of phengite (18-40%). Blueschist closer to eclogite facies exhibit higher content of omphacite and garnet up to 10% and 16%, respectively. Although blueschist from two study areas show similar mineral assemblages, samples from Jenner include much higher content of garnets (8–16%) than the samples from Ring Mountain (<2%).

Chapter 4. Analytical methods

4.1. Determination of chemical compositions of minerals

We analyzed chemical compositions of major minerals (glaucophane, epidote, phengite, omphacite, garnet, and chlorite) in the samples from Jenner (2089 and 2090) and from Ring Mountain (2097) by using electron probe micro-analyzer (EPMA, SHIMADZU 1600) at Korea Basic Science Institute (KBSI), Jeonju, Korea. The working conditions were accelerating voltage of 15 kV, beam current of 20 nA, and beam size of 1 μm for Si, Ti, Al, Cr, Fe, Mn, Mg, Ca, Na, Ni, and K. We treated the results shown as oxide weight percentages with Minpet 2.02 to identify chemical formula of each minerals.

Table 1. Modal composition of blueschist and eclogite

Sample	Study area	Rock type	Mineral modal composition (%)							
			Gln	Ep	Phg	Omp	Chl	Spn	Grt	Etc
2100	Ring Mountain	blueschist	51	37	-	2	1	7	2	-
2097		blueschist	38	49	13	-	-	-	-	-
2099-1		blueschist	73	2	8	6	2	8	1	-
2425		blueschist	39	7	40	4	7	-	3	-
2099-2		eclogite	8	33	-	51	-	3	5	-
2091	Jenner	blueschist	55	28	-	4	-	5	8	-
2089S		blueschist	58	3	2	-	4	15	10	8
2089L		blueschist	37	1	28	10	8	8	8	-
2090S		blueschist	43	1	29	3	6	2	16	-
2090L		blueschist	46	4	18	3	10	9	10	-
2088		eclogite	40	2	7	25	5	12	8	1

4.2. Measurement of LPOs of minerals

We determined the foliation of samples by well-develope4.3d schistosity and made thin sections of the foliation plane to determine the lineation. The lineation was determined by measuring grain shape of elongated minerals on the foliation using the projection-function method (Panozzo, 1984). We made thin-sections (30~50μm) of XZ plane (X: lineation-parallel and Z: foliation-normal) for each samples and polished under 1 μm diamond paste and SYTON (0.06 μm colloidal silica) to clean surface. Afterwards, thin-sections were coated with carbon to prevent charging in the operation of scanning electron microscope (SEM). LPO of minerals were measured using electron backscattered diffraction (EBSD) system with channel 5 software. The device is attached to scanning electron microscope (SEM, JEOL JSM-6380) in Seoul National University (SNU). The LPO measurements were conducted with an accelerating voltage of 20kV, a working distance of 15mm and spot size of 60 with 70˚ specimen tilt.

Fabric strength of minerals in each samples is shown as misorientation index (M-index, Skemer et al., 2005). It is defined as $M \equiv \frac{1}{2} \int | R^T(\theta) - R^O(\theta) | d\theta$, where $R^T(\theta)$ is the theoretical distribution of misorientation angles with random fabric and $R^O(\theta)$ is the distribution of observed misorientation angles. Individual misorientation angles were calculated from EBSD results.

4.3. Calculation of rock seismic properties

The P-wave seismic anisotropy (AV_P) is defined as 200 ($V_{Pmax} - V_{Pmin}$) / ($V_{Pmax} + V_{Pmin}$). Similarly, the maximum S-wave seismic anisotropy (max.AV_S) is described using this formula 200 ($V_{S1} - V_{S2}$) / ($V_{S1} + V_{S2}$). V_{S1} and V_{S2}, two orthogonally polarized S-waves, are fast and slow velocities, respectively. In this study, seismic properties of glaucophane, epidote, phengite, omphacite and whole rocks were calculated based on the single crystal elastic constants, LPOs, crystal density, and mineral modal proportions using the Voigt-Reuss-Hill (VRH) averaging scheme and David Mainprice's petro-physical software (Mainprice, 1990). I used the single crystal elastic constants (C_{ij}) of glaucophane (Bezacier et al., 2010), epidote (Ryzhova et al., 1966), phengite (Vaughan and Guggenheim, 1986), garnet (Jiang et al., 2004) and omphacite (Bhagat et al., 1992) respectively.

Chapter 5. Results

5.1. Microstructure

The blueschist samples from Ring Mountain and Jenner are relatively

coarse grained which is a representative character of Franciscan high grade blocks included in blocks-in-mélange and strongly deformed resulting in well-developed foliation and lineation (Figure 3A). Anhedral glaucophane has a grain size ranging from 100 to 700 μm in length. Very elongated epidote has subhedral to euhedral grain shape and large grain size (up to 1500μm), commonly forming layers (Figure 3A). Phengite-rich blueschist is shown in Figure 3B. Most phengites which are flaky mineral show needle shape and are aligned sub-parallel to lineation in matrix. Some phengites fill the pressure shadow of garnet grains with chlorite and the garnet grains are partially or completely chloritized. Phengites are also observed as inclusion in garnets. Therefore, phengite in the studied blocks may be occurred during prograde and retrograde process. Garnet-rich blueschist collected from Jenner, therefore, showed relatively weaker lineation than the blueschist from Ring Mountain. Two samples from Jenner Headlands (#2089, 2090) show bimodal grain size distribution showing distinct layers, therefore, we subdivided these thin-sections into large grain size layer (2089L, 2090L) and small grain size layer (2089S, 2090S). In large grain size layer, grain size of garnets ranges up to 2000 μm while that of garnet and glaucophane are both 100–200 μm in small grain size layer. The core of large garnet grains contain a lot of inclusions of most minerals comprising epidote-blueschist such as glaucophane, rutile, titanite, epidote, omphacite, and phengite. The rim of large garnet grains and small garnets, however, show no inclusions. Small grain size layers include higher content of garnet than large grain size layers.

The area proportion of small grain size layers are 5% and 13% for sample 2089 and 2090, respectively, in each thin sections. Eclogite samples are mainly composed of greenish omphacite, garnet and epidote or glaucophane (Figure 3C). Omphacite showed diverse range of grain size up to 3000 μm. The other minerals such as glaucophane and epidote showed similar microstructures in blueschist. Therefore, compositional layers of blueschist and eclogite occurred as not only distinction of colors between blue and green, but also distinction of grain size between glaucophane and omphacite.

5.2. Chemical compositions of minerals

We analyzed mineral chemical compositions of glaucophane, garnet, epidote, phengite, chlorite and omphacite in the three samples (2089 and 2090 from Jenner, 2097 from Ring Mountain) using the EPMA. The results of chemical compositions of each minerals are shown in Table 4A-F. Glaucophane, a sodic amphibole, was previously defined by $(Na + K)_A < 0.50$, $Mg / (Mg + Fe^{2+}) \geq 0.5$, and $^{6}Al \geq Fe^{3+}$ (Hawthorne et al., 1997). Some analyzed spots were identified as glaucophane (9 for 20 points). Other spots were located in the sodic-calcic amphibole field (barroisite and magnesiokatophorite) and the calcic amphibole field (actinolite and magnesiohornblende) (Table 4A). Some grains showed different amphibole

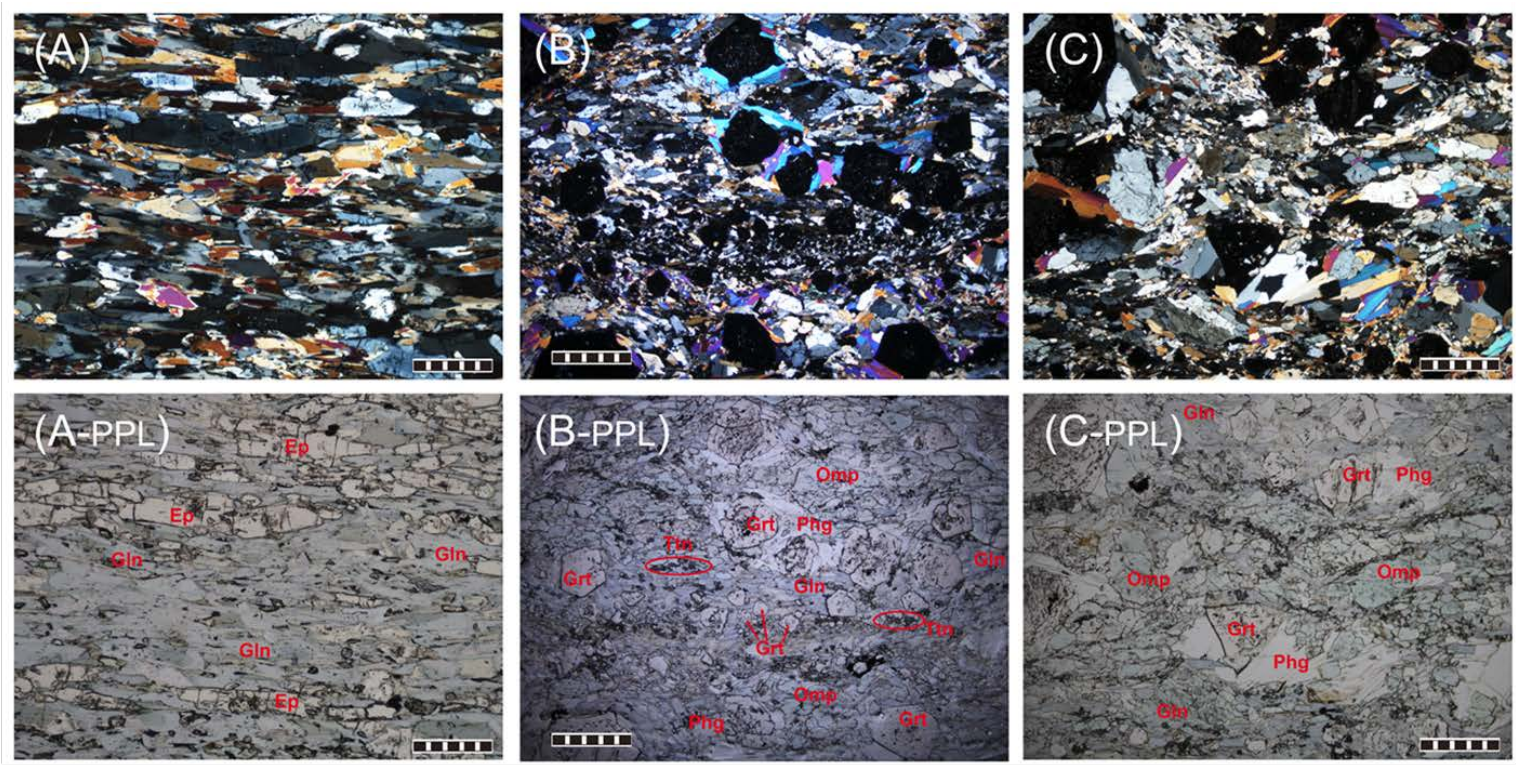

Figure 3. Optical photomicrograph of samples. (A, B, and C) Cross-polarized images. (A-, B-. and C-PPL) Plane-polarized optical images of (A, B, and C) respectively. (A) Epidote-blueschist from Ring Mountain (sample 2100) (B) Phengite-rich blueschist from Jenner (sample 2090) (C) Ecloigite from Jenner (sample 2088).

composition from core to rim. Ferric iron was calculated according to the charge-balance method described by Robinson et al. (1982). Both ferric and ferrous iron are assigned so that the total cation charge is 46. As shown in Table 4B, almandine (Fe^{2+}-rich garnet) was the highest content in all spots of garnets (52–65%). Fe^{3+} and endmembers of garnet are calculated according to the method suggested by Knowles (1987) and by Rickwood (1968), respectively. FeO of epidote group minerals was converted to Fe_2O_3 (Table 4C). We calculated mole fraction (X) of the representative end members (tawmawite, clinozoisite, and epidote; Franz, 2004). Some Fe^{3+}-rich grains in samples from Jenner were epidote (Ps = 0.2) and analyzed spots in a sample from Ring Mountain were close to clinozoisite (Ps = 0.1). The euhedral porphyroblastic grains in chloritized garnet of sample 2089 from Jenner also plotted in Mg^{2+}-rich clinozoisite field. Omphacite in sample from Jenner showed higher FeO content (6.48–7.79 %) than in sample from Ring Mountain (4.51–5.03 %; Table 4D). Fe^{3+} was estimated by charge balance method. Chlorite and phengite showed higher Mg# in the samples from Ring Mountain (69–81) than the samples from Jenner (50–74; Table 4E and F).

Table 4A. Chemical composition of amphibole in samples

Sample	Jenner															Ring Mountain				
	2089	2089	2089	2089	2089	2089	2089	2089	2089	2090	2090	2090	2090	2090	2090	2097	2097	2097	2097	2097
Mineral	Sodic				S-C	S	Calcic		Sodic-Calcic			S		S-C	S		C		S-C	
SiO_2	54.71	55.38	54.76	54.71	48.40	54.63	51.79	49.01	48.54	48.74	50.14	54.01	53.16	47.42	54.84	56.97	52.40	46.69	50.34	46.73
TiO_2	0.02	0.02	0.04	0.03	0.17	0.07	0.03	0.27	0.18	0.26	0.18	0.02	0.05	0.19	0.02	0.02	0.12	0.29	0.18	0.29
Al_2O_3	10.52	9.27	9.77	9.79	8.16	9.66	3.36	9.44	8.61	10.41	9.10	10.27	10.92	9.97	10.30	11.75	5.95	13.67	9.01	13.14
FeO	13.87	13.97	13.55	13.25	12.83	13.45	13.66	11.92	13.47	11.86	12.88	13.42	10.66	12.35	12.95	8.45	9.08	9.34	9.27	9.34
Cr_2O_3	0.05	0.02	0.08	0.03	0.02	-	0.05	0.06	0.11	0.02	0.02	-	0.01	0.04	0.03	0.02	0.02	0.01	0.05	0.01
MnO	0.14	0.18	0.14	0.15	0.14	0.14	0.28	0.06	0.15	0.03	0.10	0.13	0.08	0.08	0.11	0.13	0.19	0.20	0.21	0.23
MgO	7.87	8.61	8.39	8.63	12.41	8.46	13.64	12.60	11.58	12.20	11.55	8.48	9.91	11.60	8.51	11.52	16.33	13.41	15.21	13.49
CaO	0.96	1.98	1.58	1.67	9.35	1.53	10.71	7.91	8.98	7.39	7.49	1.90	1.47	7.19	1.27	1.71	10.17	9.58	9.45	9.56
Na_2O	7.11	6.46	6.78	6.73	3.10	6.74	1.66	4.21	3.56	4.47	4.31	6.54	6.99	4.59	6.83	7.04	2.59	3.89	3.25	4.01
K_2O	0.01	0.03	0.02	0.03	0.20	0.01	0.13	0.30	0.20	0.29	0.23	0.03	0.02	0.25	0.02	0.02	0.09	0.37	0.18	0.36
Total	95.26	95.93	95.10	95.01	94.78	94.69	95.31	95.77	95.38	95.69	95.99	94.79	93.26	93.68	94.87	97.62	96.94	97.44	97.15	97.17
Numbers of ions on the basis of 23 O																				
Si	7.850	7.912	7.883	7.872	7.190	7.889	7.668	7.144	7.207	7.092	7.318	7.794	7.693	7.084	7.867	7.782	7.437	6.671	7.134	6.710
Al	1.778	1.559	1.656	1.659	1.428	1.642	0.585	1.621	1.506	1.783	1.563	1.746	1.862	1.753	1.740	1.890	0.993	2.299	1.503	2.220
Ti	0.002	0.002	0.004	0.003	0.019	0.008	0.004	0.029	0.020	0.029	0.020	0.002	0.005	0.022	0.003	0.002	0.012	0.032	0.019	0.031
Cr	0.006	0.002	0.009	0.003	0.003	-	0.006	0.007	0.013	0.003	0.002	-	0.001	0.005	0.004	0.002	0.002	0.002	0.006	0.002
$Fe3^+$	0.235	0.208	0.181	0.190	0.245	0.201	0.166	0.311	0.107	0.353	0.157	0.238	0.321	0.353	0.224	0.170	0.283	0.218	0.390	0.171
$Fe2^+$	1.429	1.461	1.451	1.405	1.348	1.423	1.525	1.143	1.565	1.090	1.415	1.381	0.969	1.190	1.330	0.795	0.795	0.898	0.709	0.951
Mn	0.017	0.022	0.017	0.018	0.018	0.017	0.035	0.007	0.019	0.003	0.013	0.016	0.010	0.010	0.013	0.015	0.023	0.024	0.025	0.028
Mg	1.683	1.833	1.800	1.850	2.749	1.820	3.011	2.738	2.564	2.646	2.512	1.823	2.138	2.583	1.820	2.345	3.455	2.857	3.213	2.887
Ca	0.148	0.304	0.243	0.257	1.488	0.236	1.699	1.235	1.428	1.152	1.171	0.294	0.227	1.151	0.195	0.250	1.546	1.467	1.434	1.471
Na	1.979	1.790	1.891	1.879	0.893	1.888	0.476	1.189	1.026	1.262	1.219	1.830	1.960	1.329	1.899	1.866	0.714	1.076	0.894	1.117
K	0.002	0.006	0.004	0.005	0.038	0.003	0.025	0.055	0.038	0.054	0.042	0.006	0.004	0.047	0.003	0.004	0.017	0.067	0.032	0.065
Cations	15.129	15.099	15.138	15.140	15.419	15.127	15.200	15.479	15.492	15.467	15.432	15.129	15.191	15.527	15.097	15.120	15.277	15.610	15.360	15.654

Ferric iron in Amp is recalculated according to the charge-balance method described by Robinson et al. (1981)
S: sodic, S-C: sodic-calcic, and C: calcic amphibole

Table 4B. Chemical composition of garnet in samples

Sample	Jenner											
	2089	2089	2089	2089	2090	2090	2090	2090	2090	2090	2090	2090
Mineral	Garnet											
SiO_2	37.68	37.59	37.66	37.68	37.24	37.66	37.42	37.71	37.41	37.62	37.48	37.56
TiO_2	0.08	0.03	0.22	0.08	0.26	0.10	0.06	0.06	0.09	0.14	0.14	0.13
Al_2O_3	21.07	21.10	20.93	21.22	20.64	21.16	21.28	21.22	20.81	21.15	21.01	20.85
Cr_2O_3	0.01	-	0.03	0.03	0.04	-	0.01	0.04	0.01	0.08	0.02	-
FeO	27.51	26.93	27.87	27.31	24.08	26.24	27.25	26.83	26.43	25.98	26.84	26.58
MnO	0.63	0.34	3.99	0.57	6.30	0.89	0.42	0.69	1.00	0.79	1.28	1.35
MgO	2.75	2.59	1.61	2.66	1.45	3.22	0.69	2.94	2.99	2.75	2.24	2.26
CaO	9.61	10.06	9.03	9.47	9.44	9.47	9.45	9.66	9.40	10.41	10.11	9.92
Na_2O	0.01	0.01	0.03	0.03	0.01	0.02	-	0.03	0.09	0.01	-	0.02
Total	99.34	98.64	101.36	99.04	99.45	98.77	96.56	99.18	98.23	98.93	99.11	98.68
Numbers of ions on the basis of 12 O												
Si	2.999	3.010	2.974	3.007	2.993	3.002	3.092	2.999	3.003	2.999	2.997	3.016
Ti	0.004	0.002	0.013	0.005	0.015	0.006	0.004	0.004	0.006	0.008	0.008	0.008
Al	3.950	3.978	3.892	3.988	3.908	3.974	4.142	3.976	3.936	3.970	3.958	3.944
Cr	0.001	-	0.002	0.002	0.002	-	-	0.003	0.001	0.005	0.001	-
Fe^{3+}	0.091	0.090	0.092	0.091	0.081	0.087	0.094	0.089	0.089	0.086	0.090	0.089
Fe^{2+}	1.740	1.713	1.749	1.731	1.537	1.662	1.789	1.695	1.685	1.645	1.705	1.696
Mn	0.042	0.023	0.267	0.039	0.429	0.060	0.029	0.047	0.068	0.053	0.087	0.092
Mg	0.326	0.309	0.190	0.317	0.174	0.382	0.085	0.349	0.358	0.327	0.267	0.271
Ca	0.820	0.863	0.764	0.810	0.813	0.809	0.836	0.823	0.808	0.889	0.866	0.854
Na	0.002	0.001	0.004	0.005	0.001	0.004	-	0.004	0.014	0.002	-	0.004
Cations	8	8	8	8	8	8	8	8	8	8	8	8
Alm	59.435	58.903	58.894	59.773	52.059	57.057	65.314	58.19	57.723	56.446	58.31	58.242
And	4.691	4.649	4.648	4.717	4.109	4.503	5.155	4.592	4.556	4.455	4.602	4.597
Gross	23.263	25.017	20.985	23.163	23.304	23.248	25.361	23.515	23.094	25.783	24.945	24.715
Pyrope	11.13	10.631	6.392	10.929	5.887	13.124	3.09	11.965	12.272	11.216	9.122	9.291
Spess	1.439	0.8	8.98	1.332	14.528	2.061	1.063	1.605	2.32	1.828	2.962	3.156
Uvaro	0.042	0	0.101	0.085	0.113	0.006	0.018	0.133	0.036	0.272	0.058	0
X_{Cagnt}	0.28	0.297	0.257	0.28	0.275	0.278	0.305	0.282	0.277	0.305	0.296	0.293
X_{Fegnt}	0.594	0.589	0.589	0.598	0.52	0.571	0.653	0.582	0.577	0.565	0.583	0.582
X_{Mggnt}	0.111	0.106	0.064	0.109	0.059	0.131	0.031	0.12	0.123	0.112	0.091	0.093
Fe_Mg gnt	5.337	5.544	9.205	5.461	8.833	4.351	21.047	4.857	4.707	5.031	6.386	6.258

Fe^{3+} and endmembers of garnet are calculated according to the method suggested by Knowles (1987) and by Rickwood (1968), respectively.

Table 4C. Chemical composition of epidote in samples

Sample	Jenner										Ring Mountain			
	2089	2089	2089	2089	2089	2089	2090	2090	2090	2090	2097	2097	2097	2097
Mineral	Cz	Cz	Cz	Cz	Ep	Ep	Ep	Ep	Ep	Ep	Cz	Cz	Cz	Cz
SiO_2	38.10	37.98	37.89	37.95	38.78	38.29	38.17	38.05	37.93	37.95	38.94	38.56	38.82	38.48
TiO_2	0.06	0.07	0.07	0.06	0.18	0.13	0.19	0.13	0.12	0.16	0.18	0.14	0.14	0.12
Al_2O_3	24.83	25.35	25.24	25.34	26.95	25.77	26.88	25.84	26.23	24.19	29.17	28.50	29.29	28.56
Cr_2O_3	0.04	0.01	0.01	0.05	0.03	0.04	-	-	0.02	0.01	0.09	0.14	0.09	0.05
FeO	4.85	3.63	4.24	3.49	7.65	8.74	8.11	9.19	9.07	10.93	4.72	5.93	5.19	6.04
MnO	0.46	0.54	0.54	0.62	0.07	0.02	0.01	-	0.01	0.27	0.14	0.18	0.17	0.14
MgO	2.35	2.77	2.48	2.87	0.06	0.09	0.06	0.09	0.09	0.01	0.04	0.05	0.12	0.02
CaO	22.89	23.01	23.12	22.95	24.02	23.85	24.00	23.74	23.89	23.63	24.82	24.44	24.59	24.54
Na_2O	0.14	0.14	0.15	0.17	-	-	-	-	-	0.02	-	-	-	-
Total	93.72	93.49	93.73	93.51	97.73	96.93	97.41	97.05	97.37	97.16	98.10	97.95	98.41	97.95
Numbers of ions on the basis of 12.5 O														
Si	3.075	3.066	3.057	3.064	3.011	3.009	2.979	2.989	2.972	2.999	2.995	2.980	2.978	2.975
Al^{IV}	-	-	-	-	-	-	0.021	0.011	0.028	0.001	0.005	0.020	0.022	0.025
Al^{VI}	2.360	2.410	2.398	2.410	2.464	2.385	2.450	2.380	2.392	2.250	2.637	2.574	2.625	2.575
Ti	0.004	0.004	0.004	0.004	0.01	0.008	0.011	0.008	0.007	0.009	0.011	0.008	0.008	0.007
Cr	0.002	0.001	0.001	0.003	0.002	0.002	-	-	0.001	-	0.005	0.009	0.005	0.003
Fe^{3+}	0.327	0.245	0.286	0.235	0.496	0.574	0.529	0.603	0.594	0.721	0.303	0.383	0.333	0.390
Mn	0.032	0.037	0.037	0.043	0.005	0.002	-	-	0.001	0.018	0.009	0.012	0.011	0.009
Mg	0.283	0.334	0.298	0.346	0.007	0.010	0.007	0.011	0.010	0.001	0.004	0.006	0.013	0.002
Ca	1.980	1.990	1.999	1.986	1.998	2.008	2.007	1.999	2.005	2.000	2.045	2.023	2.021	2.032
Na	0.022	0.022	0.023	0.026	-	-	-	-	-	0.003	-	0.001	-	-
K	-	-	-	-	-	0.001	-	-	-	-	-	-	-	-
Cations	8.085	8.109	8.103	8.117	7.993	7.999	8.004	8.001	8.01	8.002	8.014	8.016	8.016	8.018
Ps	0.1	0.1	0.1	0.1	0.2	0.2	0.2	0.2	0.2	0.2	0.1	0.1	0.1	0.1

Total Fe as Fe^{3+}

Cz: clinozoisite, Ep: epidote

Table 4D. Chemical composition of omphacite in samples

Sample	Jenner						Ring Mountain	
	2089	2089	2090	2090	2090	2090	2097	2097
Mineral	Omphacite							
SiO_2	54.43	54.11	54.14	54.57	56.28	56.47	55.80	55.87
TiO_2	0.08	0.03	0.08	0.04	0.07	0.07	0.04	0.07
Al_2O_3	9.43	8.52	9.27	9.19	9.35	8.65	6.70	10.77
FeO	7.64	7.57	7.79	6.48	6.56	7.71	5.03	4.51
Cr_2O_3	0.01	-	-	0.03	0.03	0.05	0.05	-
MnO	0.02	0.22	0.02	0.03	-	0.03	0.17	0.14
NiO	-	0.04	-	0.01	-	-	-	0.03
MgO	7.49	7.57	7.46	7.92	7.87	7.46	10.85	8.40
CaO	12.83	14.60	13.00	13.53	13.55	13.52	17.70	13.67
Na_2O	7.34	6.49	7.24	7.01	7.21	7.06	4.94	7.17
K_2O	-	-	-	-	-	-	-	-
Total	99.27	99.15	99.00	98.81	100.92	100.99	101.26	100.62
Si	1.959	1.964	1.956	1.970	1.991	2.008	1.979	1.968
Al^{IV}	0.041	0.036	0.044	0.030	0.009	-	0.021	0.032
Al^{VI}	0.358	0.328	0.350	0.361	0.380	0.362	0.258	0.414
Ti	0.002	0.001	0.002	0.001	0.002	0.002	0.001	0.002
Cr	-	-	-	0.001	0.001	0.001	0.001	-
Fe^{3+}	0.189	0.163	0.195	0.156	0.118	0.103	0.099	0.103
Fe^{2+}	0.040	0.067	0.040	0.039	0.076	0.126	0.050	0.030
Mn	0.001	0.007	0.001	0.001	-	0.001	0.005	0.004
Ni	-	0.001	-	-	-	-	-	0.001
Mg	0.402	0.410	0.402	0.426	0.415	0.395	0.573	0.441
Ca	0.495	0.568	0.503	0.523	0.514	0.515	0.673	0.516
Na	0.512	0.457	0.507	0.491	0.495	0.486	0.340	0.490
K	-	-	-	-	-	-	-	-
Cations	4	4	4	4	4	4	4	4

Ferric iron was estimated by charge-balance method

Table 4E. Chemical composition of chlorite in samples

Sample	Jenner					Ring Mountain						
	2089	2089	2090	2090	2090	2097	2097	2097	2097	2097	2097	2097
Mineral	Chloirte											
SiO_2	26.68	25.78	25.80	25.39	25.30	27.23	27.61	27.42	26.83	27.18	26.88	27.15
TiO_2	0.02	-	0.02	-	0.02	0.02	0.02	-	0.01	0.01	0.02	0.03
Al_2O_3	18.45	18.65	18.75	18.60	18.72	19.66	18.76	19.29	20.00	19.86	20.01	19.97
Cr_2O_3	0.01	0.02	0.05	0.01	0.01	0.04	0.02	0.03	0.08	0.02	0.03	0.02
FeO	24.55	23.38	25.42	24.02	24.20	16.53	17.56	16.57	16.32	16.28	16.19	15.44
MnO	0.47	0.45	0.55	0.45	0.43	0.26	0.31	0.29	0.29	0.25	0.25	0.19
MgO	15.44	16.38	14.38	15.43	15.86	22.34	22.13	22.24	21.76	22.11	22.09	23.01
CaO	0.02	0.01	0.03	0.03	-	0.02	0.04	0.04	0.04	0.03	0.02	0.01
Na_2O	-	-	-	0.04	-	-	-	-	-	-	-	-
K_2O	0.01	-	0.01	0.02	-	-	-	-	0.02	-	-	-
Total	85.64	84.68	84.99	84.00	84.53	86.09	86.45	85.88	85.34	85.73	85.49	85.82
Numbers of ions on the basis of 36 O												
Si	5.747	5.599	5.643	5.587	5.535	5.578	5.667	5.633	5.543	5.582	5.538	5.546
Ti	0.002	-	0.003	0.001	0.003	0.003	0.003	-	0.001	0.002	0.004	0.004
Al	4.680	4.770	4.828	4.819	4.823	4.743	4.535	4.667	4.866	4.803	4.855	4.805
Cr	0.002	0.003	0.008	0.002	0.001	0.006	0.003	0.005	0.013	0.003	0.005	0.004
Fe^{2+}	4.422	4.246	4.649	4.42	4.428	2.832	3.013	2.847	2.821	2.797	2.789	2.638
Mn	0.086	0.082	0.102	0.085	0.079	0.045	0.054	0.05	0.05	0.043	0.044	0.032
Mg	4.958	5.303	4.688	5.062	5.173	6.825	6.771	6.812	6.704	6.769	6.784	7.006
Ca	0.004	0.003	0.008	0.008	-	0.004	0.009	0.009	0.009	0.006	0.004	0.003
Na	-	-	-	0.015	-	-	-	-	-	-	-	-
K	0.002	-	0.001	0.007	0.001	0.001	0.001	-	0.005	-	-	0.001
Cations	19.903	20.006	19.93	20.006	20.043	20.037	20.056	20.023	20.012	20.005	20.023	20.039
Fe#	0.47	0.44	0.5	0.47	0.46	0.29	0.31	0.29	0.3	0.29	0.29	0.27
Mg#	0.53	0.56	0.5	0.53	0.54	0.71	0.69	0.71	0.7	0.71	0.71	0.73

5.3. LPOs of minerals

In this study, LPOs of glaucophane showed different patterns between Ring Mountain and Jenner (Figure 4). Glaucophane in samples from Ring Mountain showed that [001] axes are aligned sub-parallel to lineation and both (110) pole and [100] axes are aligned normal to foliation with or without a girdle sub-normal to lineation. In contrast, samples from Jenner exhibited that [001] axes form a girdle sub-parallel to lineation except one sample, 2090S. It showed that [001] axes are aligned sub-perpendicular to lineation in the foliation. (110) pole and [100] axes display similar patterns to those of Ring Mountain, but more scattered. The fabric strength of samples from Ring Mountain (M=0.117–0.208) was stronger than that from Jenner (M=0.061–0.096). The M-index values are shown in Table 2.

As shown in Figure 5, The LPO of omphacite in eclogite showed similar patterns to glaucophane. The longest [001] axes were aligned sub-parallel to lineation. (110) and (010) poles are aligned normal to foliation with and without girdle sub-normal to lineation, respectively. The fabric strength of this mineral was also stronger in the sample from Ring Mountain (M= 0.124) than that of Jenner (M= 0.088). The LPO of omphacite in blueschist showed that [001] axes have a maxima aligning sub-normal to lineation with a girdle parallel to foliation. (110) and (010) poles also were aligned normal to

foliation, and [100] axes were very scattered.

Contrary to glaucophane, LPO patterns and fabric strength of epidote were similar in two study areas (Figure 6). They showed that [001] axes are aligned sub-normal to foliation, and both (110) and (010) poles are aligned sub-parallel to lineation, with or without a girdle parallel to foliation. The M-index values were 0.148–0.171.

The LPOs of phengite were characterized by a maximum of [001] axes normal to the foliation, with (110) and (010) poles, and [100] axes aligning in a weak girdle parallel to foliation (Figure 7). Samples from Jenner showed weaker fabric strength (M-index=0.072–0.193) than sample from Ring Mountain (M-index = 0.202), and sample 2090S, especially, showed the lowest fabric strength among phengite.

Samples from Jenner (garnet-rich blueschist) and eclogite included abundant garnet grains. The LPOs of garnet showed nearly random fabric in all samples (Figure 8).

Table 2. Fabric strength of minerals in each sample is shown as misorientation index (M-index, Skemer et al., 2005).

Sample	Study area	Rock type	Gln	Ep	Phg	Omp
2100	Ring Mountain	blueschist	0.155	0.171	-	-
2097		blueschist	0.173	0.148	-	-
2099-1		blueschist	0.208	-	-	-
2425		blueschist	0.117	-	0.202	-
2099-2		eclogite	-	0.157	-	0.124
2091	Jenner	blueschist	0.078	0.159	-	-
2089S		blueschist	0.078	-	-	-
2089L		blueschist	0.069	-	0.093	0.182
2090S		blueschist	0.073	-	0.072	-
2090L		blueschist	0.096	-	0.193	-
2088		eclogite	0.061	-	-	0.088

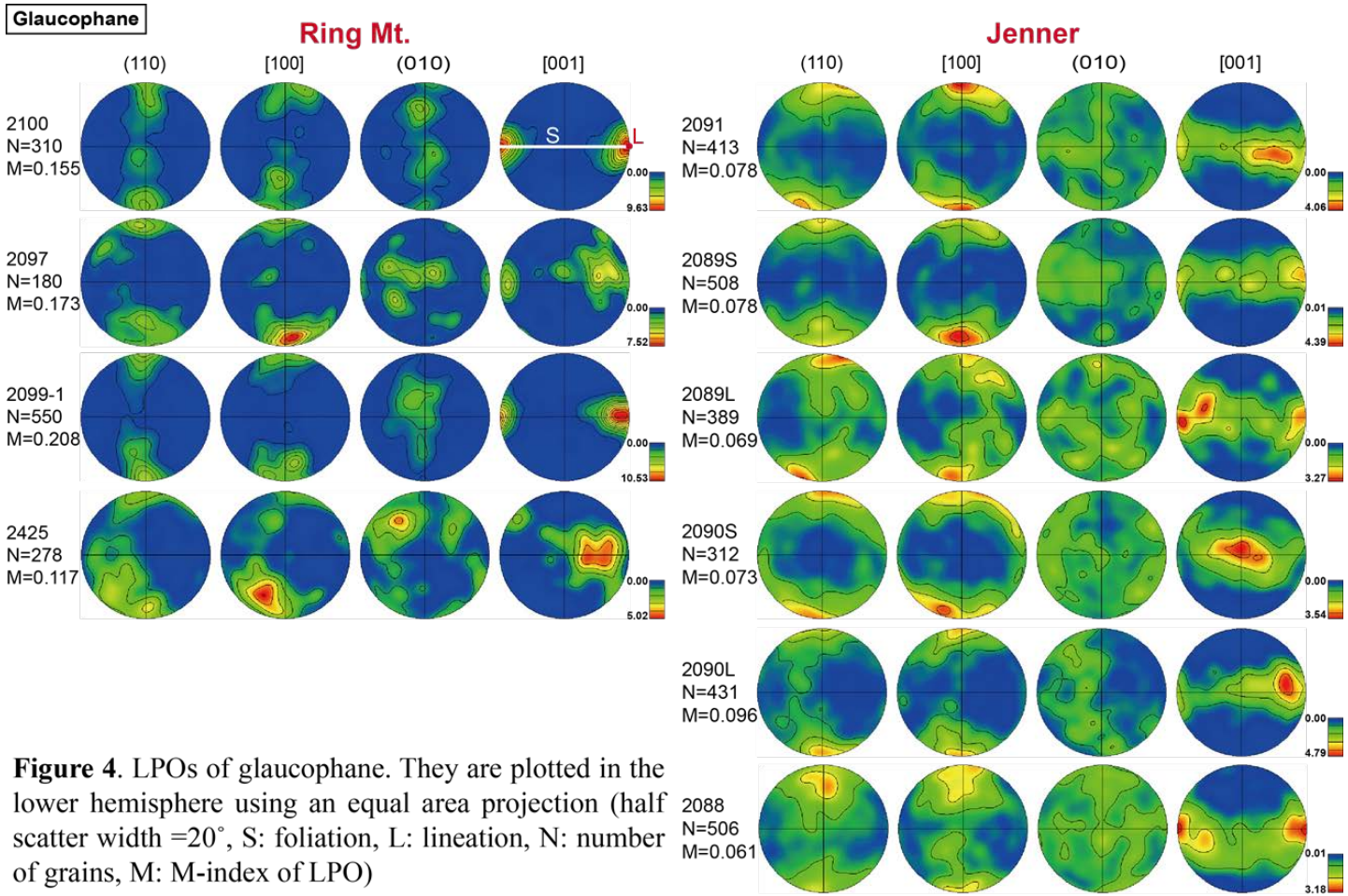

Figure 4. LPOs of glaucophane. They are plotted in the lower hemisphere using an equal area projection (half scatter width =20˚, S: foliation, L: lineation, N: number of grains, M: M-index of LPO)

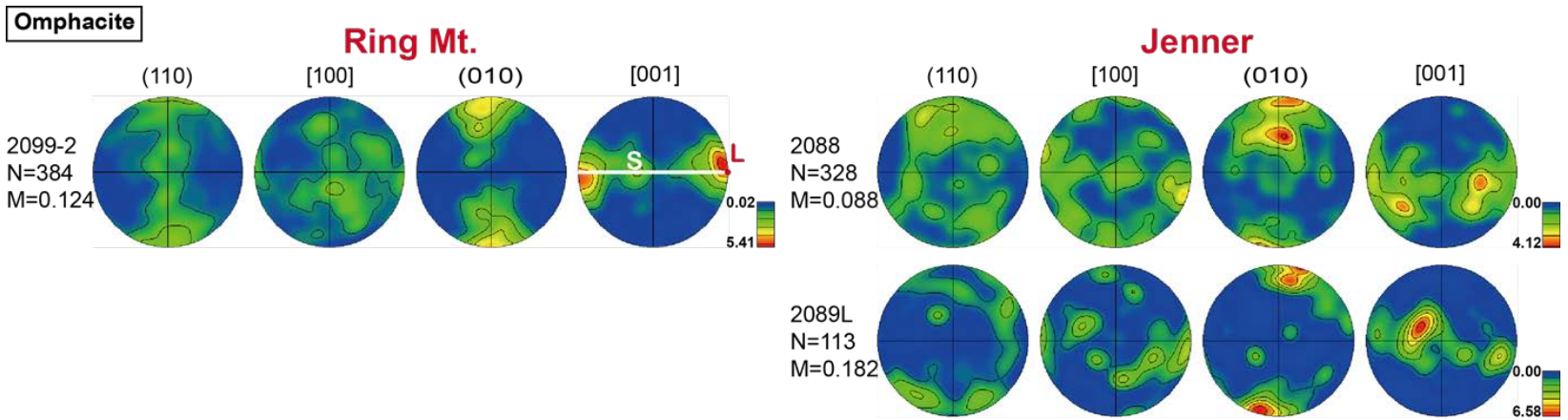

Figure 5. LPOs of omphacite. They are plotted in the lower hemisphere using an equal area projection (half scatter width =20˚, S: foliation, L: lineation, N: number of grains, M: M-index of LPO)

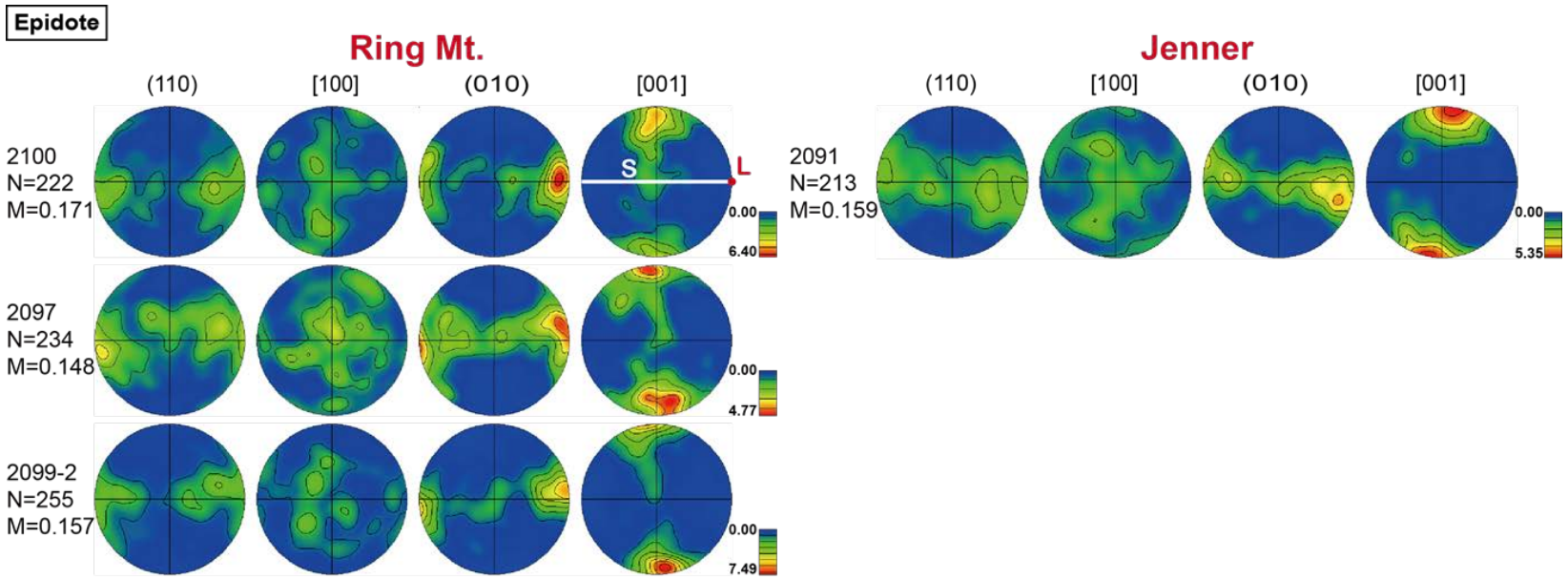

Figure 6. LPOs of epidote. They are plotted in the lower hemisphere using an equal area projection (half scatter width =20˚, S: foliation, L: lineation, N: number of grains, M: M-index of LPO)

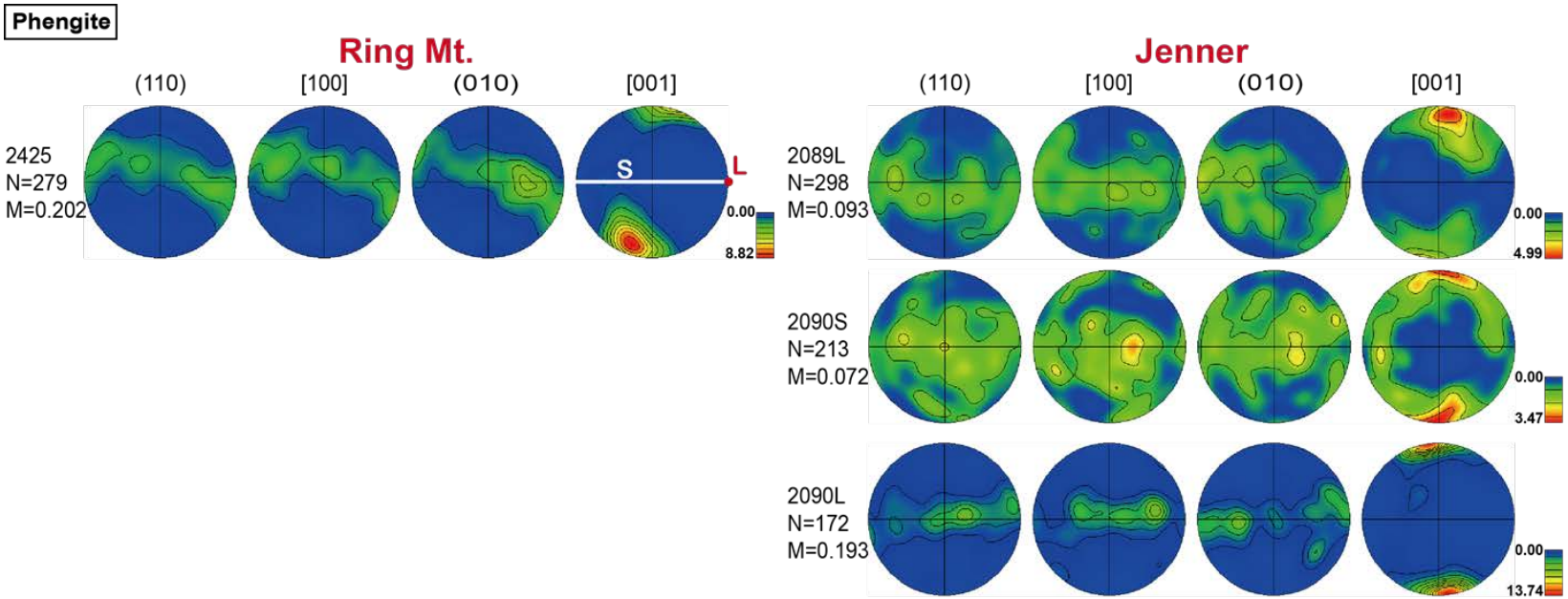

Figure 7. LPOs of phengite. They are plotted in the lower hemisphere using an equal area projection (half scatter width =20˚, S: foliation, L: lineation, N: number of grains, M: M-index of LPO)

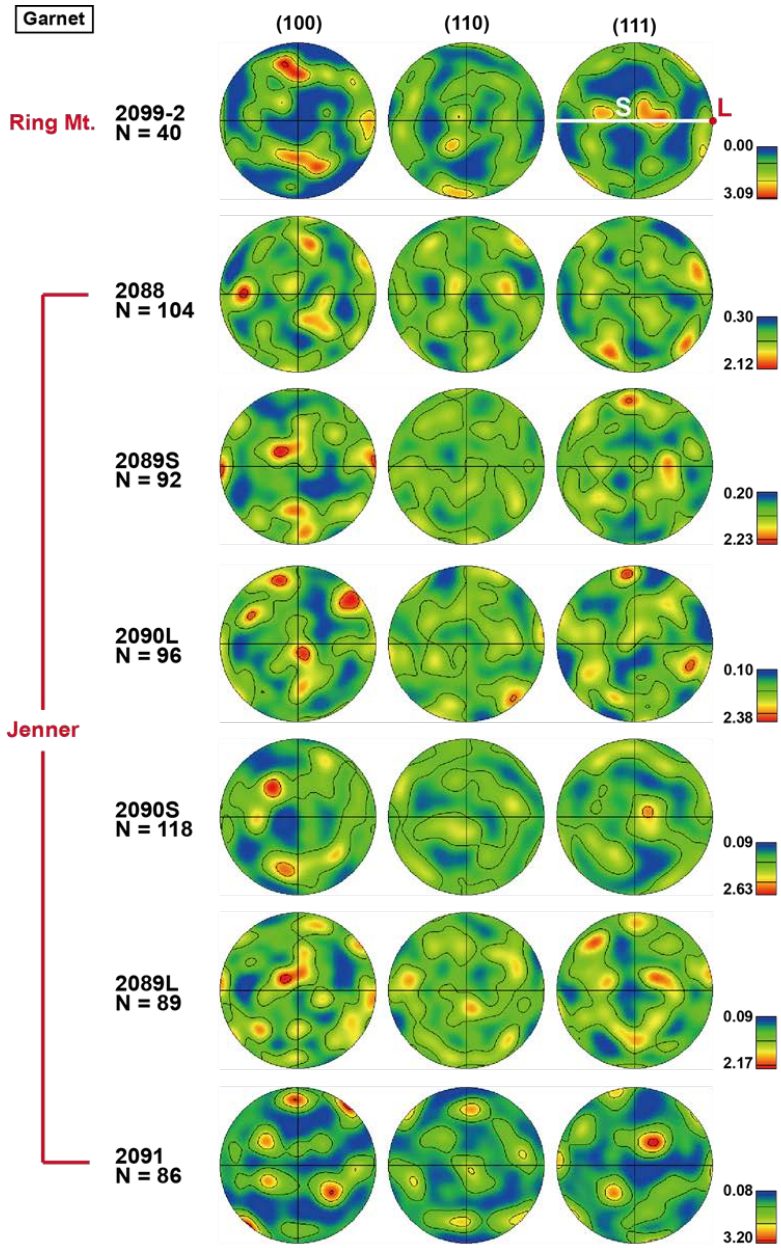

Figure 8. LPOs of garnet. They are plotted in the lower hemisphere using an equal area projection.
(half scatter width =20˚, S: foliation, L: lineation, N: number of grains)

5.4. Seismic velocity and anisotropy of minerals

In this study, we calculated seismic properties for major minerals such as glaucophane, epidote, phengite, omphacite, and garnet. For calculating of whole rocks, we used normalized mineral assemblages of Gln + Ep (or Phg) for Ring Mountain epidote-blueschist, Gln + Phg (or Ep) + Grt ± Omp for Jenner garnet-rich blueschist, and Omp + Ep (or Gln) + Grt for eclogite (Table 3).

As shown in Figure 9, seismic anisotropy of glaucophane, likewise fabric strength, was stronger in the samples from Ring Mountain (AV_P=17–22%, max.AVs=9–12%) than those from Jenner (AV_P=11–15%, max.AVs=7–9%). The slowest P-wave velocities of glaucophane in both area are sub-normal to foliation. Faster V_P show lower angles to foliation. Similarly, stronger polarization anisotropies were aligned at lower angles to the foliation than weaker polarization anisotropies. When the shear wave propagates normal to foliation, the direction of V_{S1} polarization showed diverse directions in the foliation according to LPOs of [001] axes. Therefore, glaucophane of samples from Ring Mountain generally showed that the polarization direction of fast shear wave is aligned sub-parallel to the lineation. On the other hand, samples from Jenner which showed foliation-parallel [001] axes with a girdle exhibited the directions between X and Y (X: lineation-parallel direction, Y:

Table 3. Seismic anisotropy of P- and S-waves for major minerals and whole rocks

sample	Study area	Rock type	Gln (%)		Ep (%)		Phg (%)		Omp (%)		Grt (%)		Whole rock	
			AV_P	AV_{Smax}	AV_P	AV_{Smax}	AV_P	AV_{Smax}	AV_P	AV_{Smax}	AV_P	AV_{Smax}	AV_P	AV_{Smax}
2100	Ring Mountain	blueschist	17.2	9.3	8.2	9.83	-	-	-	-	-	-	13.2	8.82
2097		blueschist	19.3	12.41	7.6	9.80	-	-	-	-	-	-	12.1	9.61
2099-1		blueschist	22.3	12.44	-	-	-	-	-	-	-	-	22.3	12.44
2425		blueschist	18.3	9.96	-	-	41.9	37.47	-	-	-	-	29.8	23.43
2099-2		eclogite	-	-	9.4	12.91	-	-	3.2	1.91	0.1	0.23	4.9	5.58
2091	Jenner	blueschist	14.3	8.38	7.9	11.80	-	-	-	-	0.1	0.13	10.7	8.61
2089S		blueschist	15.0	6.24	-	-	-	-	-	-	0.1	0.15	12.5	7.85
2089L		blueschist	11.4	6.88	-	-	27.4	20.63	3.2	3.06	0.0	0.10	14.2	9.61
2090S		blueschist	14.7	7.30	-	-	20.3	17.85	-	-	0.1	0.15	13.4	9.37
2090L		blueschist	13.1	8.88	-	-	42.1	43.49	-	-	0.1	0.15	18.3	16.80
2088		eclogite	11.1	6.79	-	-	-	-	2.4	1.74	0.0	0.06	5.9	3.95

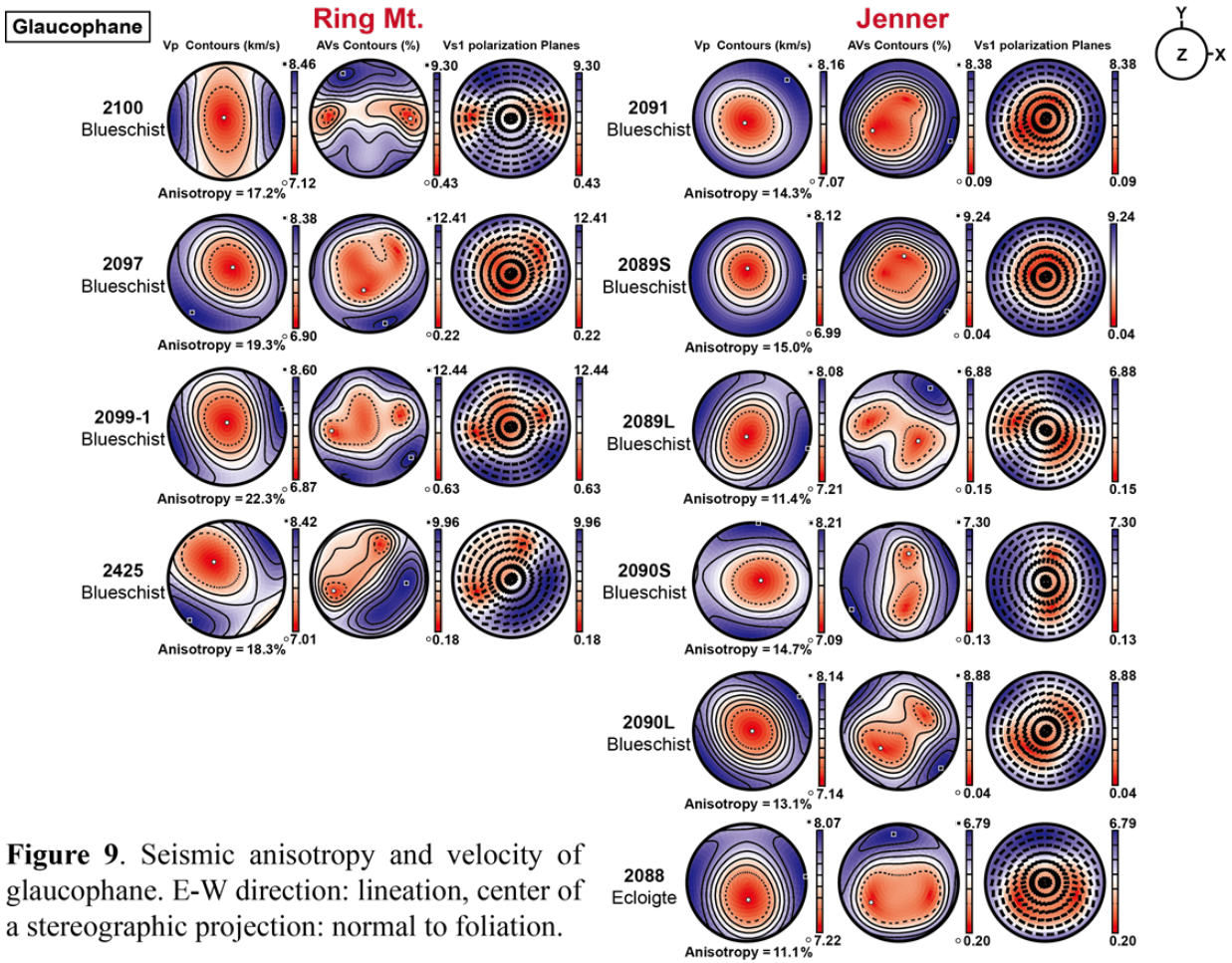

Figure 9. Seismic anisotropy and velocity of glaucophane. E-W direction: lineation, center of a stereographic projection: normal to foliation.

normal to X direction in foliation). Among them, the sample 2090S showed that V_{S1} direction is normal to lineation. The fast S-wave polarization, however, was sub-parallel to foliation when the S-wave propagates low angles to foliation in all samples.

We calculated seismic properties of omphacite in eclogite samples from both study areas and a blueschist sample (#2089L) close to eclogite facies (transitional facies) from Jenner (Figure 10). Omphacite in eclogite samples from Ring Mountain showed very low seismic anisotropy (AV_P = 3.2%, max.AV_S = 1.91%). The fastest and slowest P-wave velocities are sub-parallel and sub-normal to foliation, respectively. The polarization anisotropy patterns were very complicated. The min.V_P and max.V_P of this mineral in eclogite from Jenner are parallel and normal to lineation, respectively. Seismic anisotropy (AV_P = 2.4%, max.AV_S = 1.74%) was weaker in both P- and S-waves than that of sample from Ring Mountain. Omphacite in transitional facies blueschist from Jenner showed the strongest seismic anisotropy (AV_P = 3.2%, max.AV_S = 3.06%). The pattern of P-wave contours was similar to the sample from Ring Mountain.

Seismic anisotropy of epidote was in the range of 8–9% for P-wave and 10–13% for maximum polarization anisotropy (Figure 11). Anisotropy patterns were similar to those of glaucophane. The fastest and slowest P-wave velocities are sub-parallel to lineation and sub-normal to foliation, respectively. The strong shear-wave anisotropy was aligned at low angles to

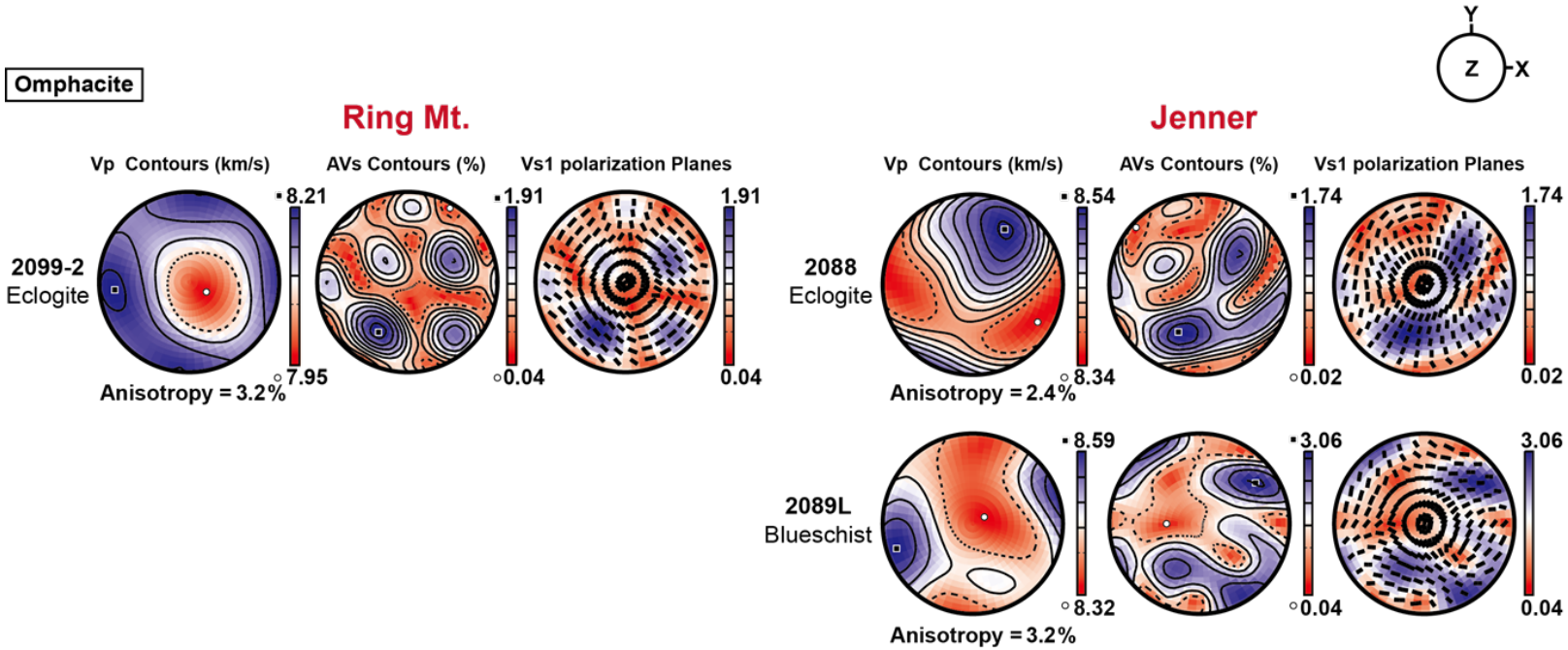

Figure 10. Seismic anisotropy and velocity of omphacite. E-W direction: lineation, center of a stereographic projection: normal to foliation.

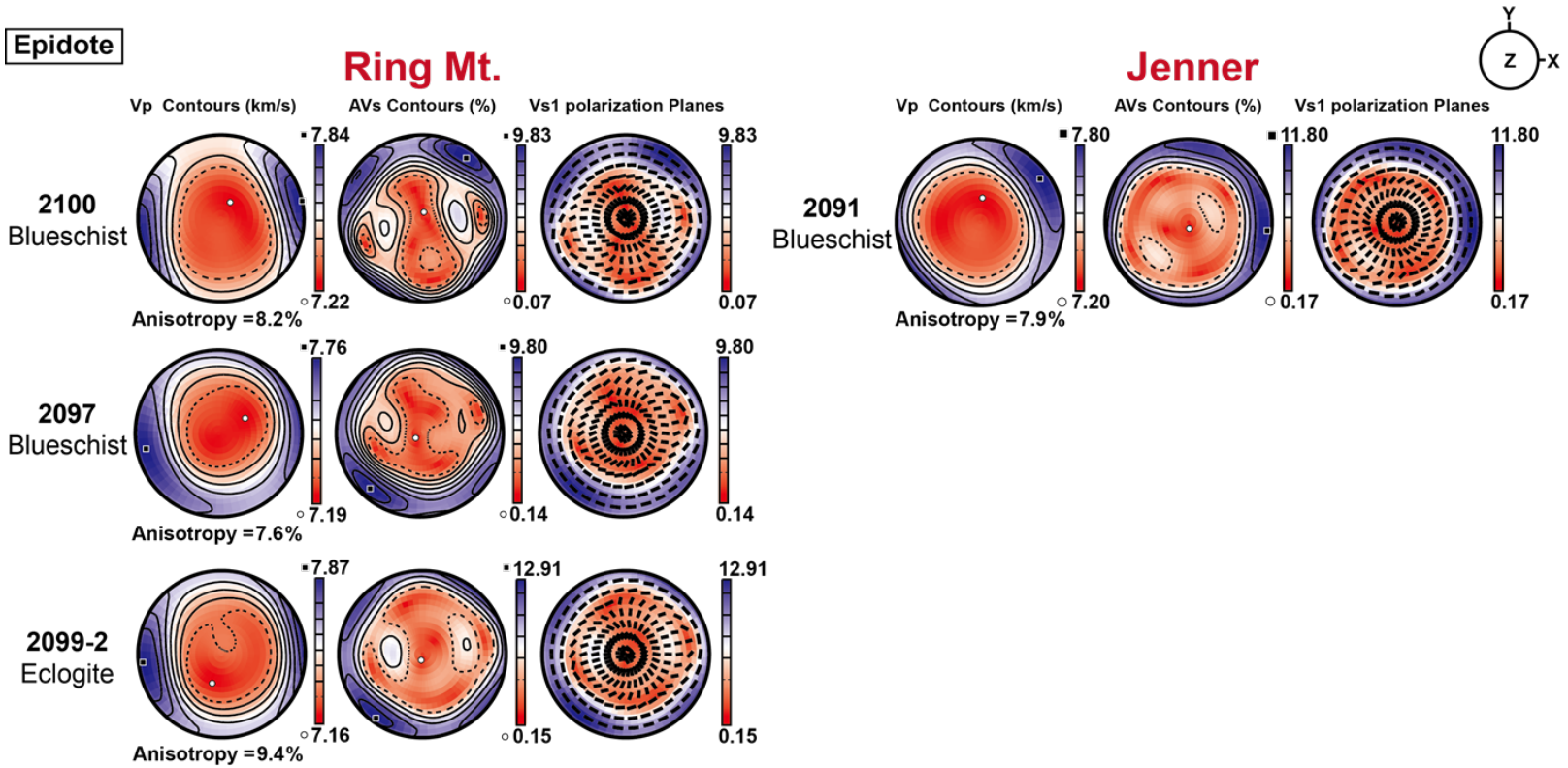

Figure 11. Seismic anisotropy and velocity of epidote. E-W direction: lineation, center of a stereographic projection: normal to foliation.

foliation, and the weak AV_S were sub-normal to foliation.

Seismic anisotropy of phengite was much stronger than those of above minerals. P-wave anisotropy was in the range of 20–42% and the maximum polarization anisotropy was in the range of 18–43% (Figure 12). The lowest seismic anisotropy was in 2090S which showed very weak fabric LPO. Anisotropic patterns of this mineral were also similar to glaucophane and epidote. The slowest V_P are normal to foliation and the fastest V_P are in the foliation. The maximum P-wave velocity of 2090S was parallel to Y-direction. The strong and weak polarization anisotropies were aligned at low and high angles to foliation, respectively. The V_{S1} polarization showed similar patterns to the fastest V_P when the incident ray propagates normal to foliation. Therefore, the direction of V_{S1} polarization is normal to lineation in sample 2090S. Whereas, the polarization direction of fast shear wave was normal to lineation when shear waves propagate at low angle to foliation in all samples.

The garnets in garnet-rich blueschist (Jenner samples) and eclogite showed much weaker seismic anisotropy (AV_P = 0.0–0.1 %, max.AV_S = 0.06–0.23 %) due to random LPO patterns and weak anisotropy of garnet single crystal (Figure 13). Seismic anisotropy for P-wave, especially, showed nearly isotropic patterns. The maximum shear-wave anisotropy was stronger in eclogite sample from Ring Mountain than those from Jenner. Among samples from Jenner, eclogite sample showed weaker polarization anisotropy than garnet-rich blueschist.

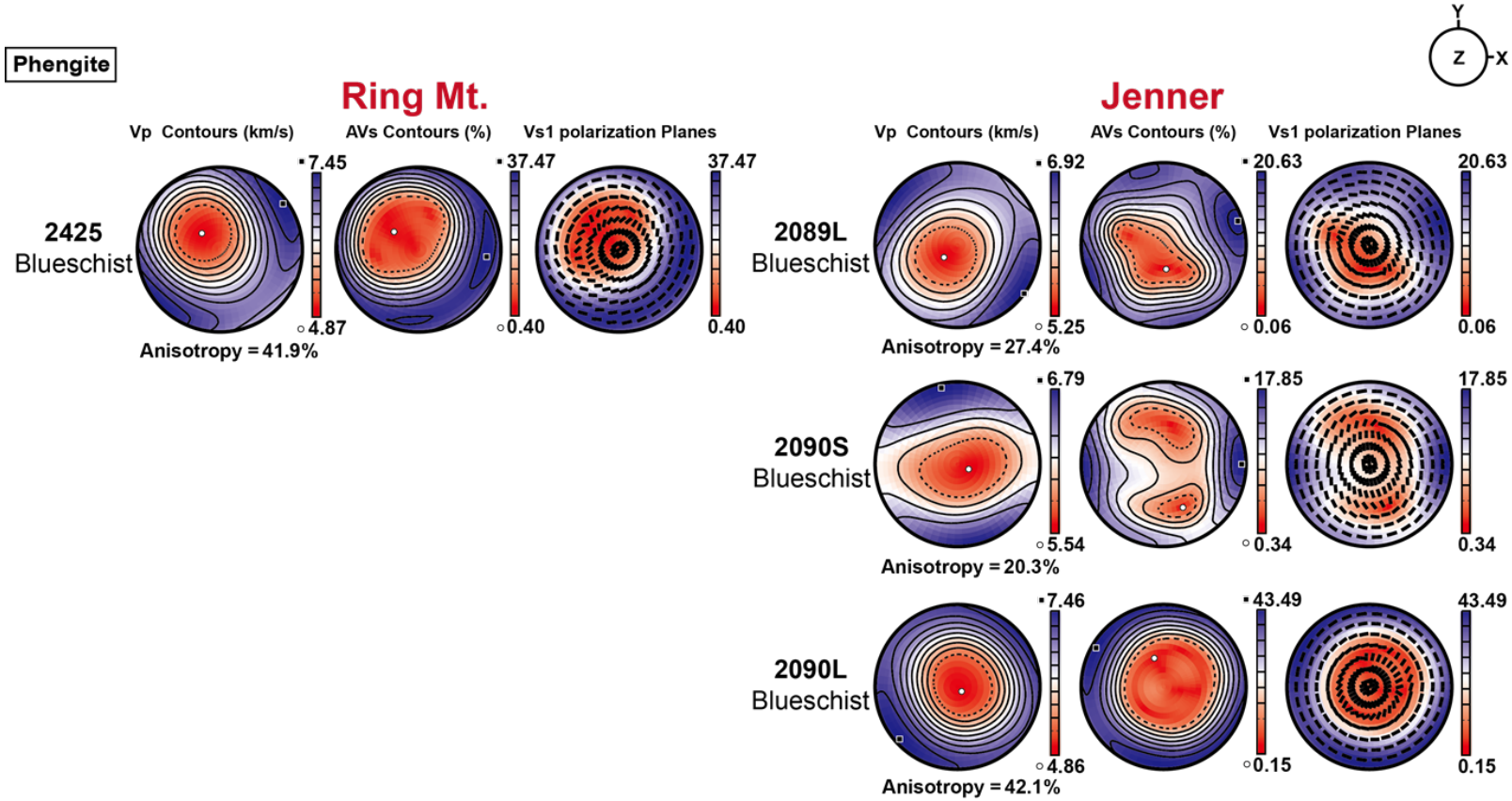

Figure 12. Seismic anisotropy and velocity of phengite. E-W direction: lineation, center of a stereographic projection: normal to foliation.

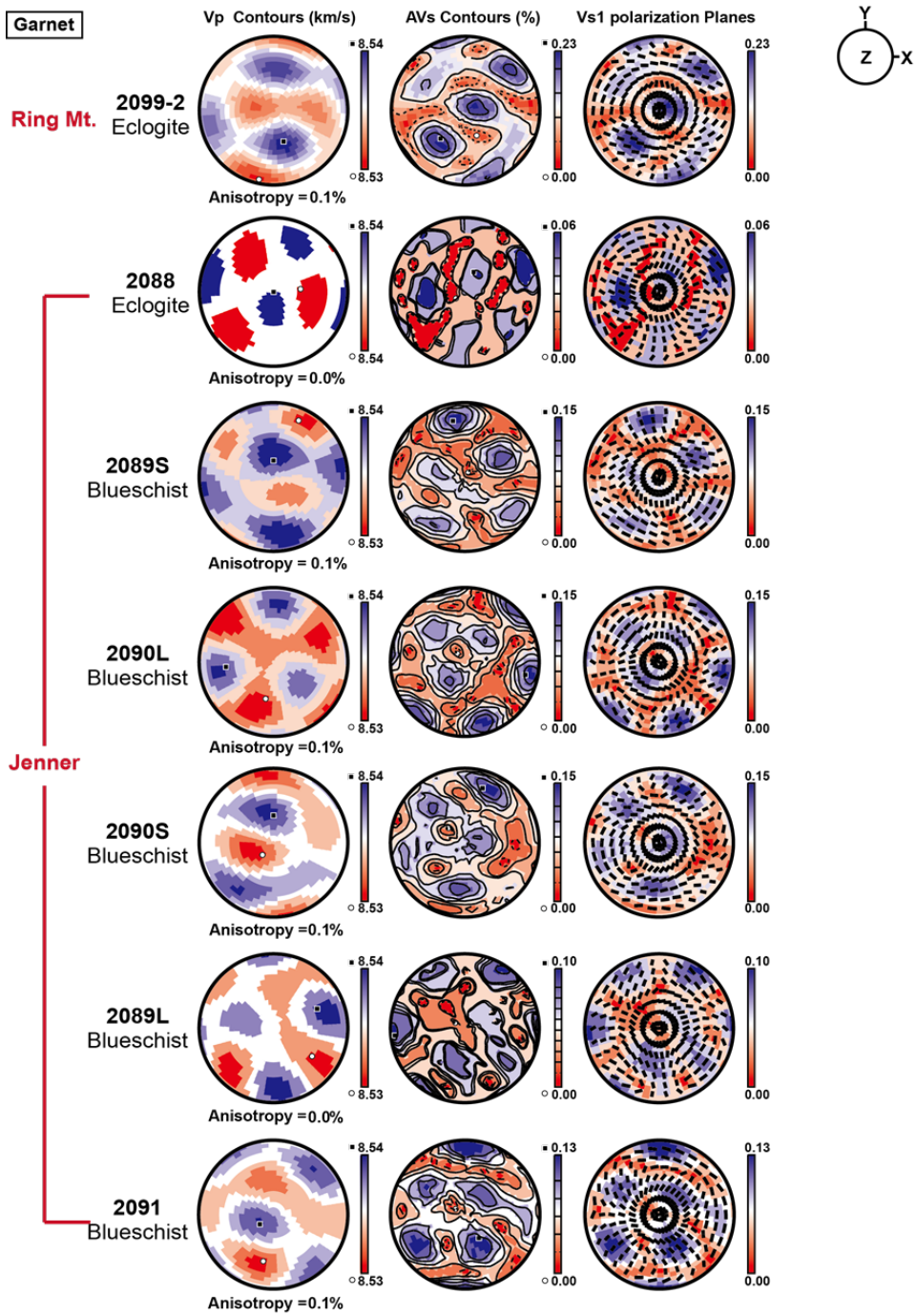

Figure 13. Seismic anisotropy and velocity of garnet. E-W direction: lineation, center of a stereographic projection: normal to foliation.

As shown in Figure 14, seismic anisotropy patterns of whole rocks resembled to mineral showing relatively higher seismic anisotropy such as glaucophane or phengite for blueschist, and glaucophane or epidote for eclogite. Faster P-wave velocity and stronger polarization anisotropy were sub-parallel to foliation, and the slowest V_P and weaker AV_S were aligned high angle to foliation in all samples. Fast shear wave polarization directions were diverse between X and Y direction when incident ray propagates normal to foliation, and normal to lineation direction when waves propagates nearly parallel to foliation, respectively. Eclogite including a lot of omphacite and garnet showed the lowest seismic anisotropy (AV_p = 4.9–5.9 %, max.AV_s = 3.95–5.58 %) among the samples. Blueschist samples, whereas, including high content of phengite showed very strong seismic anisotropy (13.4–29.8% for P-wave and 9.37–23.4% for S-wave). Seismic anisotropy of the other epidote-blueschist was 10.7–22.3% for P-wave and 7.85–12.44% for shear-wave. Epidote- and phengite-rich blueschist from Jenner showed weaker seismic anisotropy than those from Ring Mountain due to lower seismic anisotropy of glaucophane and composition of garnet ± omphacite.

We calculated seismic properties of glaucophane, phengite and whole rock of sample 2425 considering subducting angle from 0° to 70° (Figure 15A-C). When the dipping angle of subducting slab increases, polarization directions of fast shear wave changed to trench-parallel direction (Y) and seismic anisotropy of shear wave (AV_S) also changed from weak to strong in

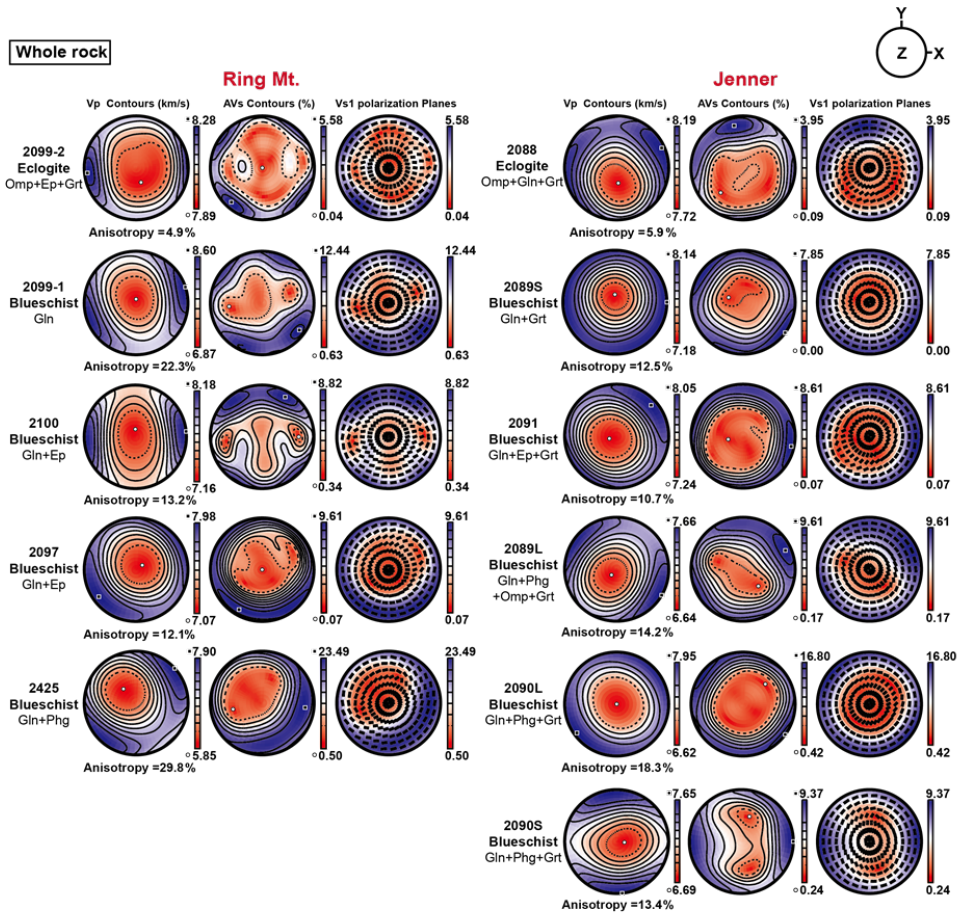

Figure 14. Seismic anisotropy and velocity of whole rocks. E-W direction: lineation, center of a stereographic projection: normal to foliation.

both minerals when the incident ray propagates vertically. Glaucophane and phengite showed weak AV_S, ~4% and ~2.9%, respectively, for the horizontal flow ($\theta = 0°$). When dipping angle of slab becomes $\theta = 30$, 45, 60, and 70°, glaucophane showed the AV_S ~7.5%, ~9.0% ~9.9%, and 9.0%, respectively (Figure 15A). Seismic anisotropy of phengite also increased with higher dipping angle. The AV_S was nearly 16%, 26%, 35%, and 37% when subducting angle is $\theta = 30$, 45, 60, and 70° (Figure 15B). We calculated seismic anisotropy of whole rock using the bi-mineralogical assemblages of glaucophane and phengite considering the modal composition 49.9% and 50.1%, respectively. Anisotropy patterns of whole rock according to variable dipping angle showed similar signature to both minerals. When slab is subducted nearly flat ($\theta = 0°$), AV_S of whole rock was weak (~3%) for vertically propagating incident ray. The AV_S became stronger with increasing dipping angle from 0° to 70° (~10.5% at $\theta = 30°$, ~17% at $\theta = 45°$, ~22% at $\theta = 60°$) and was proximate to the max.AV_S when the subducting angle became 70° (~23.5%; Figure 15C).

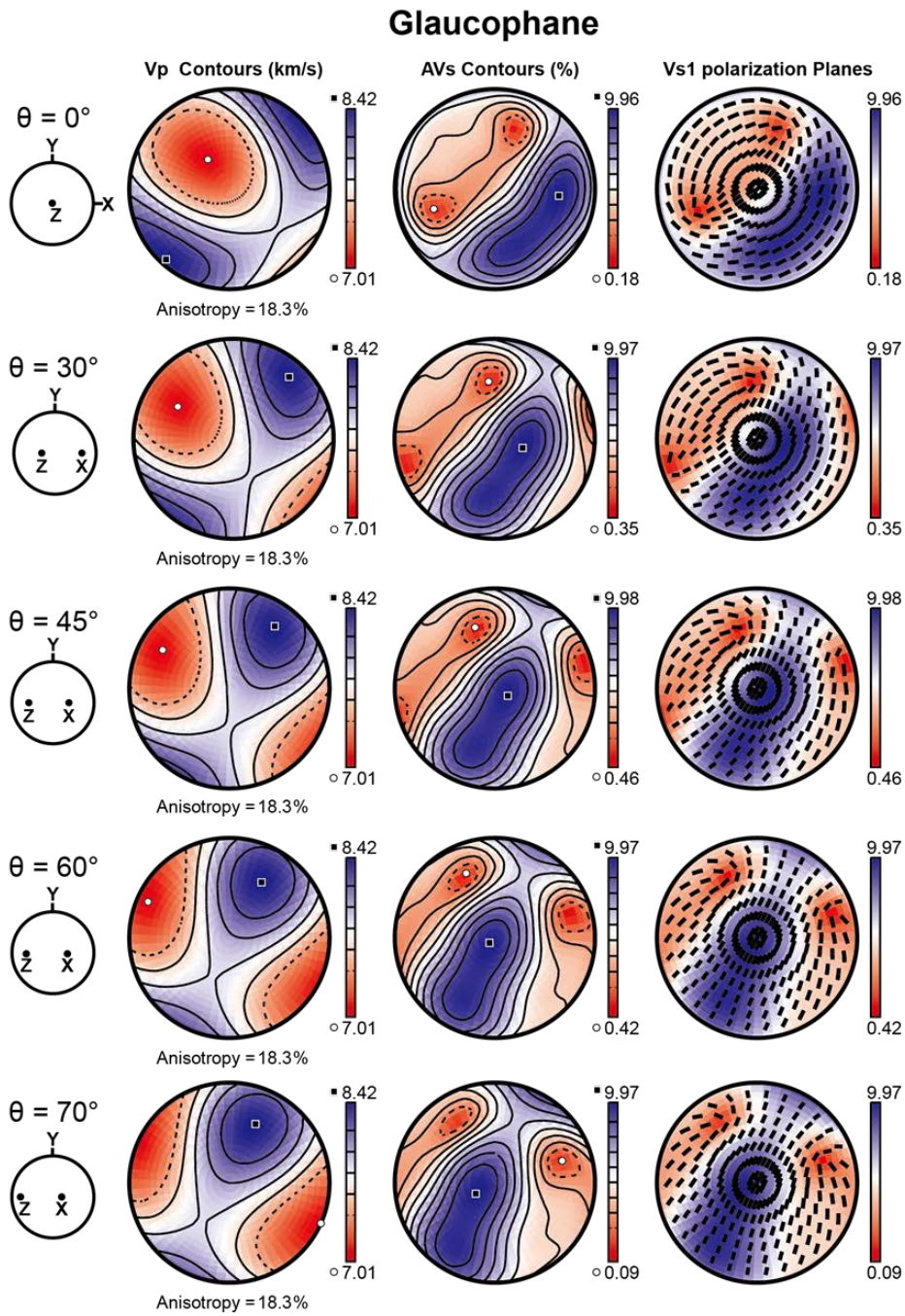

Figure 15A. Effect of dip angle (θ) on the seismic anisotropy of glaucophane in sample 2425. The X and Z directions indicate the lineation and the normal to foliation direction, respectively.

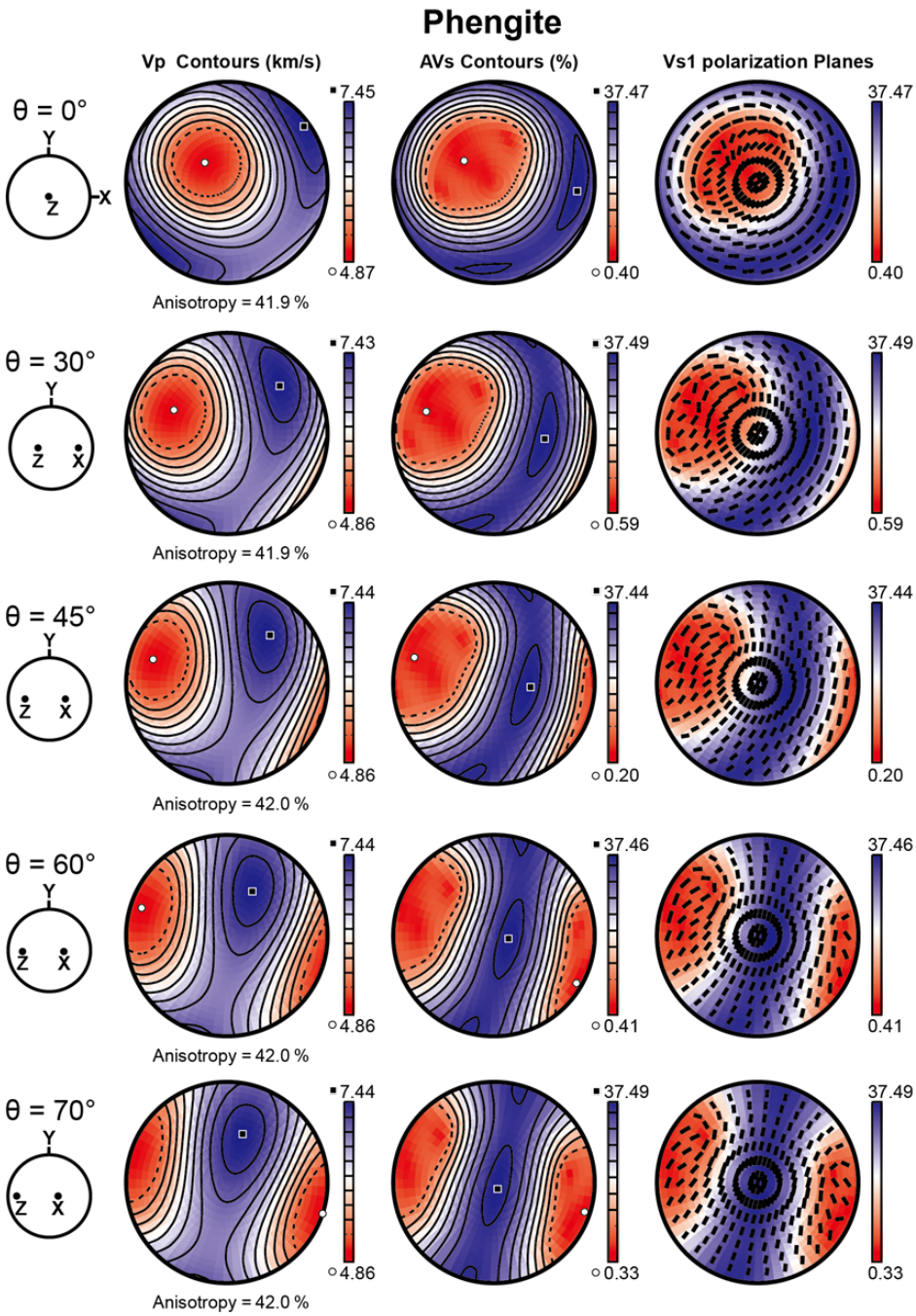

Figure 15B. Effect of dip angle (θ) on the seismic anisotropy of phengite in sample 2425. The X and Z directions indicate the lineation and the normal to foliation direction, respectively.

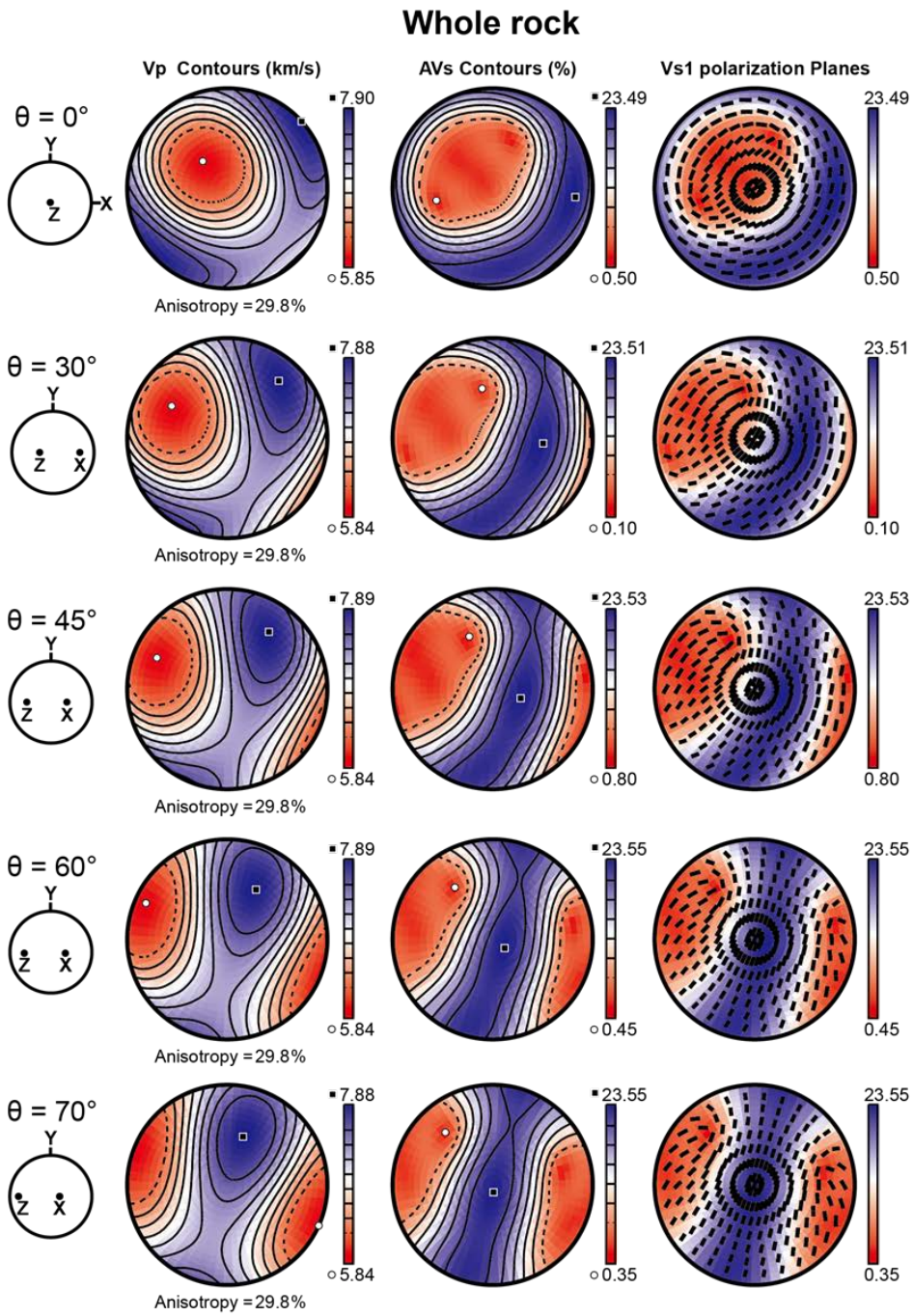

Figure 15C. Effect of dip angle (θ) on the seismic anisotropy of whole rock considering the modal proportion of glaucophane and phengite in sample 2425. The X and Z directions indicate the lineation and the normal to foliation direction, respectively.

Chapter 6. Discussion

6.1. LPO variations of minerals

6.1.1. LPO of glaucophane

The LPOs of glaucophane in samples from Ring Mountain showed that [001] axes were aligned parallel to lineation and (110) poles and [100] axes were aligned sub-normal to foliation. This LPO pattern has been reported in several previous studies (Bezacier et al., 2010; Fujimoto et al., 2010; Teyssier et al., 2010; Kim et al., 2012; Cao et al., 2013; Kim et al., 2013a, 2013b; Cao et al., 2014). Glaucophane in samples from Jenner, however, showed unusual LPO patterns in naturally deformed blueschist which is foliation-parallel [001] axes with a girdle. These glaucophanes also showed noticeable weaker fabric strength than those from Ring Mountain. The differences of fabric strength and LPO type in glaucophane are likely due to much higher content of garnet in samples from Jenner. Rigid garnet grains could affect the LPOs of soft glaucophane significantly. The LPO randomization effect of garnet has been reported in previous study of Cao et al. (2013). In that study, the LPOs of glaucophane showed that (110) poles, [100] and [010] axes were aligned normal to foliation with a girdle, and [001] axes were parallel to lineation

without a girdle. This type also showed weaker fabric strength than another usual type (SL-type). Although the LPOs of glaucophane in garnet-rich blueschist are different to the results of this study, abundant garnets could randomize [001] axes of glaucophane on the foliation plane and weaken the fabric. Most other minerals except for epidote and omphacite in blueschist from Jenner also showed weaker fabric strength than those from Ring Mountain. Uncommon LPO type of glaucophane in garnet-rich blueschist in this study also may be developed by pure shear deformation. Undergone coaxial deformation, the longest axes, [001] axes, of glaucophane in samples from Jenner were aligned relatively random on the foliation.

Small grain size layer in sample 2090 from Jenner which includes the highest content of garnet showed the LPO of glaucophane characterized by a maximum of [001] axes normal to the lineation with a girdle parallel to foliation. Bimodal grain size distribution with layers is considered at least two deformation events. Large grain size of garnets showed textural discontinuity between core and rim suggesting at least two growth stages. The core of large garnets included a lot of inclusions such as omphacite, rutile, phengite, and glaucophane, whereas, rim had no inclusions. Garnets in small grain size layer showed also clean core and rim without any inclusions. The rim of large garnet grains and small grain size of garnet, therefore, are crystallized in second growth stages after first growth of core of large garnet grains. In first stage, samples from Jenner deformed and developed the LPO patterns of

glaucophane consistent with samples from Ring Mountain. After that, deformation directions changed and developed small grain size layers showing LPO of glaucophane which [001] axes subnormal to lineation on the foliation in second growth stage. Meanwhile, large glaucophane which had been shown lineation-parallel [001] axes developed foliation-parallel [001] axes with a girdle.

6.1.2. LPO of omphacite

We measured LPOs of omphacite for two eclogite samples and one blueschist sample. The LPOs of omphacite showed different patterns among them (Figure 5). The LPO of omphacite in eclogite sample 2099-2 from Ring Mountain showed that (010) poles are aligned normal to foliation and [001] axes are aligned parallel to lineation which is called the ‘SL-type’ in several previous studies (e.g., Godard and van Roermund, 1995; Mauler et al., 2001; Brenker et al., 2002; Zhang et al., 2006). This type occurs under the simple shear deformation (Bascou et al., 2001; Zhang et al., 2006). The LPO of omphacite in transitional facies blueschist (sample 2089L) from Jenner, however, showed a maxima of (010) poles aligning normal to foliation and a maxima of [001] axes sub-normal to lineation in the foliation with a girdle parallel to foliation which is called the ‘S-type or flattening fabric. In several

previous studies of experiment and modeling, this LPO type of omphacite occurs when they undergone axial compression or transpression deformation (Bascou et al., 2001; Zhang et al., 2006). The omphacite in eclogite sample (2088) from Jenner showed relatively weak fabric strength (M = 0.088) and intermediate LPO type between sample 2099-2 and 2089L. Therefore, the omphacite also may be deformed by different deformation geometry in two study areas.

6.1.3. LPO of epidote and phengite

Epidote showed similar fabric strength between Ring Mountain and Jenner. The LPO of epidote in a sample from Jenner showed that both (110) and (010) poles are aligned parallel to foliation with a girdle (Figure 6). Samples from Ring Mountain, however, showed both (110) and (010) poles are aligned parallel to lineation, and some (010) poles form a girdle parallel to foliation. In several previous studies, epidote showed slip systems of (001)[010] (Bezacier et al., 2010; Cao et al., 2011; Cao et al., 2013; Kim et al., 2013b) and {101}[010] (Fujimoto et al., 2010; Cao et al., 2011; Cao et al., 2013). Subhedral to euhedral grain shape of epidote may be deformed slightly as a nearly rigid body in a relatively soft glaucophane matrix (Kim et al., 2013a; Cao et al., 2014). Phengite showed similar LPO type and fabric

strength between Ring Mountain and Jenner. Because phengite are observed near the garnet grains, the LPO of phengite is considered to be affected by rigid garnet mostly. Phengite in small grain size layer (2090S) showed the weakest fabric strength (M = 0.072) and [001] axes are aligned normal to foliation with a very weak girdle. Small grain size layer, therefore, may be formed with a different deformation direction and/or affected randomization by garnets.

6.2. Seismic anisotropy of epidote blueschist and eclogite in the subducting slab

Glaucophane, similarly to fabric strength, showed stronger seismic anisotropy in samples from Ring Mountain than in samples from Jenner. Garnet-rich blueschist from Jenner, also, included higher content of garnet ± omphacite which make much lower seismic anisotropy. Comparing seismic anisotropy with similar mineral assemblage, epidote- and phengite-rich blueschist, therefore, showed stronger seismic anisotropy in samples from Ring Mountain than those from Jenner.

Phengite, especially, showed the strongest seismic anisotropy and similar anisotropy patterns to glaucophane. As a result, blueschist including high content of phengite showed much stronger seismic anisotropy. Phengite-rich

blueschist from Ring Mountain which is mainly composed of glaucophane and phengite showed the strongest seismic anisotropy in both P-wave and S-wave (AV_P = 29.8%, max.AV_S = 23.43%). Although blueschist from Jenner included garnet and omphacite, samples including high content of phengite showed quite strong seismic anisotropy (AV_P = 14.2–18.3 %, max.AV_S = 9.37–16.8%). When we calculated seismic anisotropy of blueschist from Jenner using the mineral assemblage excluded garnet ant omphacite to confirm the effect of phengite, phengite-rich samples showed much stronger seismic anisotropy (AV_P = 16.8–18.3 %, max.AV_S = 11.48–19.42%) than epidote-blueschist (AV_P = 11.8–15.0 %, max.AV_S = 9.24–9.48%). Therefore, phengite can affect seismic anisotropy of whole rock significantly.

Omphacite and garnet showed much weaker seismic anisotropy. Since eclogite is mainly composed of these minerals, eclogite showed much weaker seismic anisotropy (AV_P = 4.9–5.9%, max.AV_S = 3.95–5.58) than blueschist. When we added garnet ± omphacite for calculating seismic anisotropy of whole rocks from Jenner, it decreased about 1–3% for both P-wave and S-wave. Therefore, strong seismic anisotropy observed in most subduction zone can be more affected by blueschist rather than eclogite.

In many subduction zones, the delay times of 0.1–0.3 s and 1–2 s caused by anisotropic layers are naturally observed (e.g., Polet and Kanamori, 2002; Nakajima and Hasegawa, 2004; Anglin and Fouch, 2005; Nakajima et al., 2006; Long and van der Hilst, 2006). The delay times of 1– 1.5 s have been

observed in California including Ring Mountain and Jenner (Polet and Kanamori, 2002) and we cannot rule out the anisotropy induced by remnants of Farallon plate beneath the North American plate in this area. We, therefore, calculated the delay time of an oceanic crust using the equation suggested by Pera et al. (2003)

$$\mathrm{D} = 100 \times \mathrm{dt} \times < V_S > / AV_S$$

D is the thickness of an anisotropic layer and assumed 7 km thick of homogeneous oceanic crust in this study, *dt* is the delay times, and $<V_S>$ is the average velocity of shear wave. The average V_P and V_S were calculated as $(V_{Pmax} + V_{Pmin})/2$ and $(V_{S1max} + V_{S1min} + V_{S2max} + V_{S2min})/4$, respectively (Table 5). We applied max.AV_S for AV_S, therefore, actual delay time would be smaller according to subducting angle in subduction zone. Eclogite samples showed too small delay times of 0.08–0.06 s to interpret naturally observed delay times. Whereas, blueschist showed the delay times of 0.1–0.4 s that can make a considerable effect to observed delay times in the fore-arc region. Blueschist, especially phengite- rich blueschist, can affect seismic anisotropy in subduction zones significantly with deformed mantle rocks.

Phengite-rich blueschist showed very strong seismic anisotropy in this study and oceanic crust is subducted downward with variable dipping angle in subduction zones. We, therefore, considered the subducting angle of phengite-rich blueschist (sample 2425) from flat to high angle subduction (0–70°; Figure 16A-E). Glaucophane and phengite showed oblique fast shear

Table 5. Average P- and S-wave velocities of major minerals and whole rocks

sample	Study area	Rock type	Gln (km/s)		Ep (km/s)		Phg (km/s)		Omp (km/s)		Grt (km/s)		Whole rock (km/s)	
			V_P	V_S	V_P	V_S	V_P	V_S	V_P	V_S	V_P	V_S	V_P	V_S
2100	Ring Mountain	blueschist	7.79	4.56	7.53	4.22	-	-	-	-	-	-	7.67	4.42
2097		blueschist	7.64	4.52	7.48	4.22	-	-	-	-	-	-	7.53	4.35
2099-1		blueschist	7.74	4.55	-	-	-	-	-	-	-	-	7.74	4.55
2425		blueschist	7.72	4.54	-	-	6.16	3.45	-	-	-	-	6.88	3.93
2099-2		eclogite	-	-	7.52	4.21	-	-	8.08	4.73	8.54	4.80	8.09	4.6
2091	Jenner	blueschist	7.62	4.53	7.5	4.21	-	-	-	-	8.54	4.80	7.65	4.45
2089S		blueschist	7.56	4.52	-	-	-	-	-	-	8.54	4.80	7.66	4.55
2089L		blueschist	7.65	4.55	-	-	6.09	3.52	8.46	4.88	8.54	4.80	7.15	4.17
2090S		blueschist	7.65	4.54	-	-	6.17	3.53	-	-	8.54	4.80	7.17	4.15
2090L		blueschist	7.64	4.55	-	-	6.16	3.42	-	-	8.54	4.80	7.29	4.22
2088		eclogite	7.65	4.54	-	-	-	-	8.44	4.88	8.54	4.80	7.96	4.67

wave polarization direction between X and Y when the shear waves propagate normal to foliation considering the flat subduction and seismic anisotropy of S-wave was very weak (Figure 16A). If the subducting angle of the slab increases the polarization direction changed to the trench-parallel direction (Y) and AV_S became stronger for vertically propagating S-waves (Figure 16B-E). Combining glaucophane (50%) and phengite (50%), whole rock showed similar changes of polarization direction of S-wave and AV_S since both minerals showed similar anisotropy patterns. Therefore, phengite-rich blueschist in subducting slab can contribute to strong trench-parallel seismic anisotropy depending on the dipping angle of subducting slab in subduction zones.

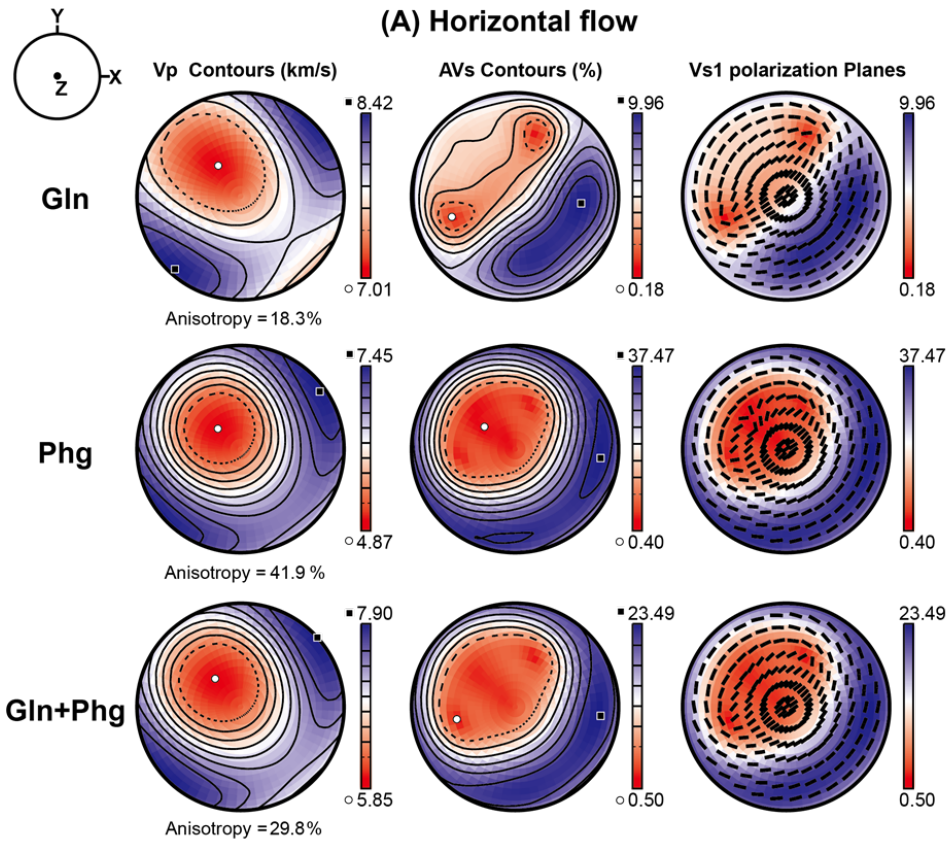

Figure 16. Effect of dip angle (θ) on the seismic anisotropy of glaucophane, phengite and whole rock of sample 2425. (A) horizontal flow. (B) flow dipping at 30°. (C) flow dipping at 45°. (D) flow dipping at 60°. (E) flow dipping at 70°. the X and Z directions indicate the lineation and the normal to foliation direction, respectively.

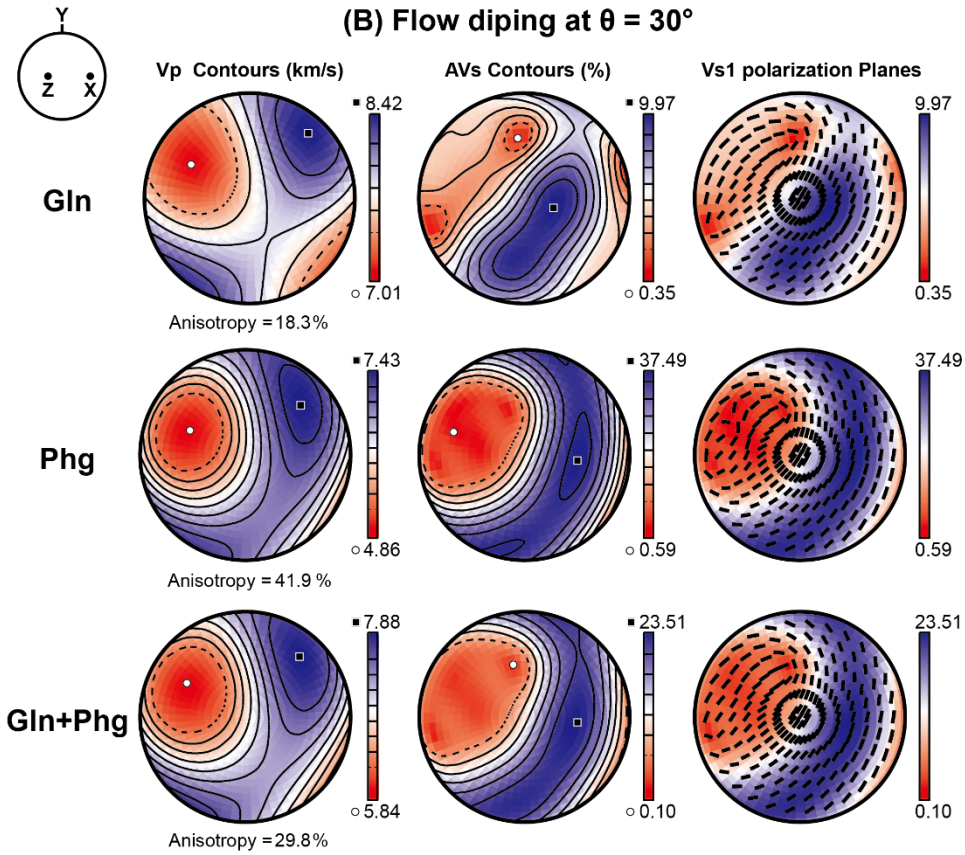

Figure 16. Continued.

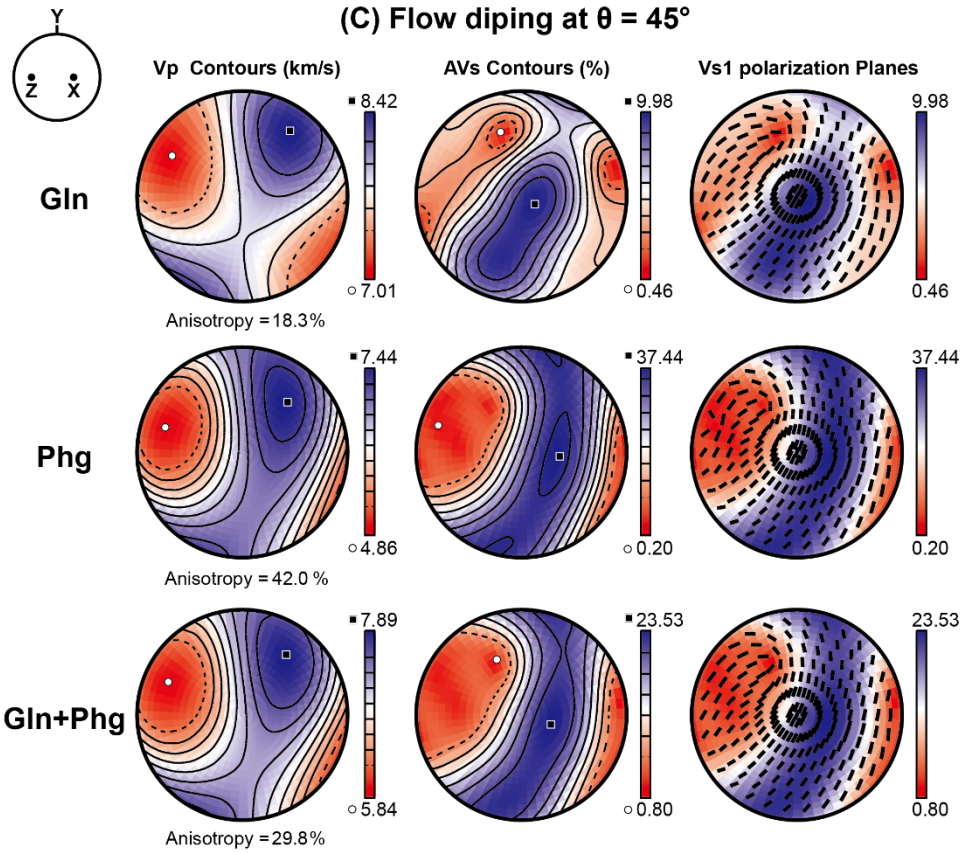

Figure 16. Continued.

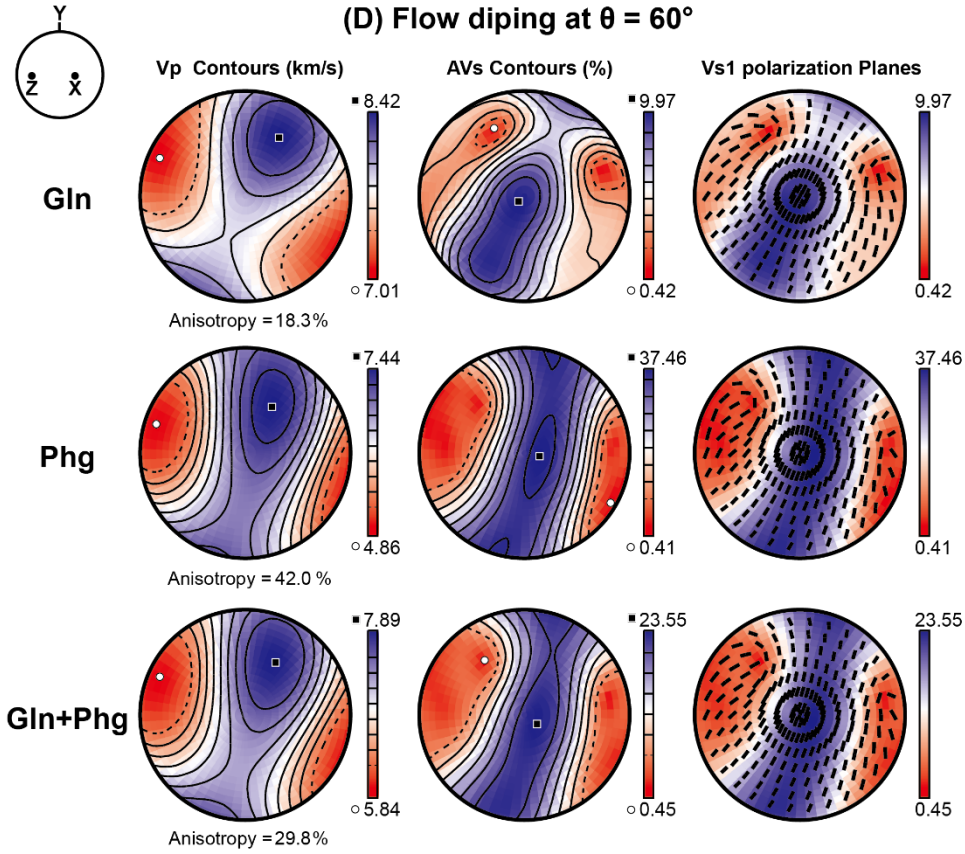

Figure 16. Continued.

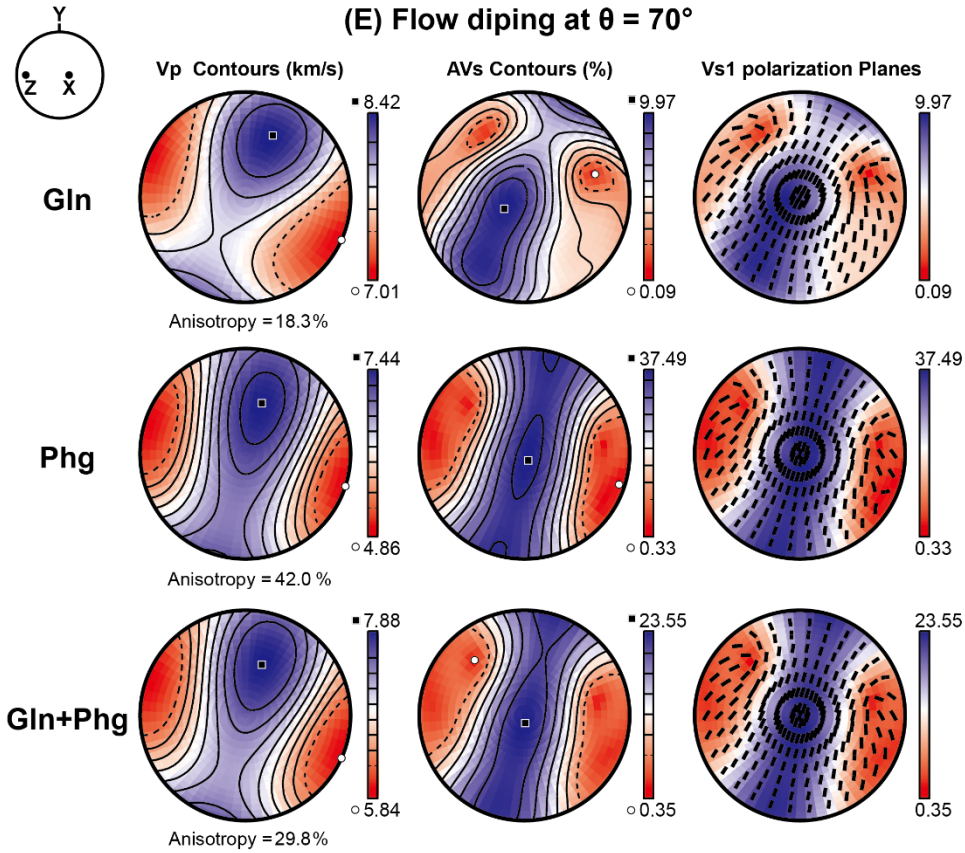

Figure 16. Continued.

Chapter 7. Conclusion

We studied microstructures and seismic properties of naturally deformed blueschist and eclogite from Jenner and Ring Mountain to understand the seismological implications of subducting oceanic crust which is transformed to blueschist or eclogite at the high pressure and low temperature conditions. In this study, we determined lattice preferred orientations (LPOs) of minerals and calculated seismic properties of major minerals and whole rocks. Glaucophane showed different LPO patterns in two study areas, and LPOs of this mineral in the samples from Jenner have not been observed in previous studies. [001] axes of glaucophane were aligned parallel to lineation in the samples from Ring Mountain, but parallel to foliation with a girdle in the samples from Jenner, and normal to lineation on the foliation in the small grain size layer. The LPO of omphacite in a sample from Ring Mountain (2099-2) showed that [001] axes are aligned parallel to lineation and (110), (010) poles are aligned normal to foliation with and without a girdle, respectively. Omphacite in a blueschist sample from Jenner, however, showed different LPO pattern characterized by a maximum of [001] axes normal to lineation on the foliation in a girdle parallel to foliation, with (110), (010) poles aligning normal to foliation. Omphacite in an eclogite sample from Jenner showed the LPO in the midway of above two LPO patterns and much weaker fabric strength. The LPOs of epidote showed that [001] axes are

aligned normal to foliation, and (110), (010) poles are aligned parallel to lineation with or without girdle parallel to foliation. The LPOs of phengite were characterized by a maximum of [001] axes normal to foliation, with (110), (010) poles, and [100] axes aligning parallel to foliation with a weak girdle. Phengite in the small grain size layer showed much weaker LPO fabric. The LPOs of garnets showed nearly random fabric in all analyzed samples.

The seismic anisotropy of blueschist showed much stronger than eclogite. Blueschist from Jenner which were including high content of garnet ± omphacite showed weaker seismic anisotropy than blueschist from Ring Mountain. Therefore, omphacite and garnet weaken the seismic anisotropy of whole rock significantly. The phengite, whereas, showed very strong seismic anisotropy, and whole rocks including abundant phengite showed much stronger seismic anisotropy than the other epidote-blueschist and eclogite. Therefore, strong seismic anisotropy observed in subduction zone can be affected by blueschist rather than eclogite. Phengite-rich blueschist, especially, can develop significant seismic anisotropy in subducting slab.

References

Agostinetti, N.P., Miller, M.S., 2014. The fate of the downgoing oceanic plate: Insight from the Northern Cascadia subduction zone. Earth and Planetary Science Letters 408, 237-251.

Anczkiewicz, R., Platt, J.P., Thirlwall, M.F., Wakabayashi, J., 2004. Franciscan subduction off to a slow start: evidence from high-precision Lu–Hf garnet ages on high grade-blocks. Earth and Planetary Science Letters 225, 147-161.

Anglin, D.K., Fouch, M.J., 2005. Seismic anisotropy in the Izu-Bonin subduction system. Geophysical Research Letters 32.

Bailey, E.H., Blake Jr, M., Jones, D.L., 1970. On-land Mesozoic oceanic crust in California coast ranges. US Geological Survey Professional Paper 700, C70-C81.

Bailey, E.H., Irwin, W.P., Jones, D.L., 1964. Franciscan and related rocks and their significance in the geology of western California, California Division of Mines and Geology, pp.

Bascou, J., Barruol, G., Vauchez, A., Mainprice, D., Egydio-Silva, M., 2001. EBSD-measured lattice-preferred orientations and seismic properties of eclogites. Tectonophysics 342, 61-80.

Bascou, J., Tommasi, A., Mainprice, D., 2002. Plastic deformation and development of clinopyroxene lattice preferred orientations in eclogites. Journal of Structural Geology 24, 1357-1368.

Berkland, J.O., Raymond, L.A., Kramer, J.C., Moores, E.M., O'Day, M., 1972. What is Franciscan? AAPG Bulletin 56, 2295a-2302.

Bezacier, L., Reynard, B., Bass, J., Wang, J., Mainprice, D., 2010. Elasticity of glaucophane, seismic velocities and anisotropy of the subducted oceanic crust. Tectonophysics 494, 201-210.

Bhagat, S.S., Bass, J.D., Smyth, J.R., 1992. Single-crystal elastic properties

of omphacite-C2/c by Brillouin spectroscopy. Journal of Geophysical Research: Solid Earth (1978–2012) 97, 6843-6848.

Blake, J., M.C., Jayko, A.S., McLaughlin, R.J., Underwood, M.B., 1988. Metamorphic and tectonic evolution of the Franciscan Complex, northern California, Metamorphism and crustal evolution of the Western United States 8, Prentice-Hall Englewood Cliffs, New Jersey, pp. 1035-1060.

Brenker, F.E., Prior, D.J., Müller, W.F., 2002. Cation ordering in omphacite and effect on deformation mechanism and lattice preferred orientation (LPO). Journal of Structural Geology 24, 1991-2005.

Cao, Y., Jung, H., Song, S., 2013. Petro-fabrics and seismic properties of blueschist and eclogite in the North Qilian suture zone, NW China: Implications for the low-velocity upper layer in subducting slab, trench-parallel seismic anisotropy, and eclogite detectability in the subduction zone. Journal of Geophysical Research: Solid Earth 118, 3037-3058.

Cao, Y., Jung, H., Song, S., 2014. Microstructures and petro-fabrics of lawsonite blueschist in the North Qilian suture zone, NW China: Implications for seismic anisotropy of subducting oceanic crust. Tectonophysics 628, 140-157.

Cao, Y., Song, S.G., Niu, Y.L., Jung, H., Jin, Z.M., 2011. Variation of mineral composition, fabric and oxygen fugacity from massive to foliated eclogites during exhumation of subducted ocean crust in the North Qilian suture zone, NW China. Journal of Metamorphic Geology 29, 699-720.

Cloos, M., 1983. Comparative study of melange matrix and metashales from the Franciscan subduction complex with the basal Great Valley Sequence, California. The Journal of Geology, 291-306.

Cloos, M., 1986. Blueschists in the Franciscan Complex of California: Petrotectonic constraints on uplift mechanisms. Geological Society of

America Memoirs 164, 77-94.

Coleman, R., Lanphere, M., 1971. Distribution and age of high-grade blueschists, associated eclogites, and amphibolites from Oregon and California. Geological Society of America Bulletin 82, 2397-2412.

Coleman, R.G., Lee, D.E., Beatty, L.B., Brannock, W.W., 1965. Eclogites and eclogites: their differences and similarities. Geological Society of America Bulletin 76, 483-508.

Currie, C.A., Cassidy, J.F., Hyndman, R.D., Bostock, M.G., 2004. Shear wave anisotropy beneath the Cascadia subduction zone and western North American craton. Geophysical Journal International 157, 341-353.

Ernst, W., 1970. Tectonic contact between the Franciscan melange and the Great Valley sequence—crustal expression of a late Mesozoic Benioff zone. Journal of Geophysical Research 75, 886-901.

Ernst, W., 1988. Tectonic history of subduction zones inferred from retrograde blueschist PT paths. Geology 16, 1081-1084.

Ernst, W., 2011. Accretion of the Franciscan Complex attending Jurassic–Cretaceous geotectonic development of northern and central California. Geological Society of America Bulletin 123, 1667-1678.

Fouch, M.J., Fischer, K.M., 1996. Mantle anisotropy beneath northwest Pacific subduction zones. Journal of Geophysical Research: Solid Earth (1978–2012) 101, 15987-16002.

Franz, G., Liebscher, A., 2004. Physical and Chemical Properties of the Epidote Minerals–An Introduction–. Reviews in mineralogy and geochemistry 56, 1-81.

Fujimoto, Y., Kono, Y., Hirajima, T., Kanagawa, K., Ishikawa, M., Arima, M., 2010. P-wave velocity and anisotropy of lawsonite and epidote blueschists: Constraints on water transportation along subducting oceanic crust. Physics of the Earth and Planetary Interiors 183, 219-228.

Godard, G., van Roermund, H.L., 1995. Deformation-induced clinopyroxene fabrics from eclogites. Journal of Structural Geology 17, 1425-1443.

Hacker, B.R., Abers, G.A., Peacock, S.M., 2003. Subduction factory 1. Theoretical mineralogy, densities, seismic wave speeds, and H2O contents. Journal of Geophysical Research: Solid Earth (1978–2012) 108.

Hamilton, W., 1969. Mesozoic California and the underflow of Pacific mantle. Geological Society of America Bulletin 80, 2409-2430.

Hawthorne, F.C., Kato, A., Kisch, H.J., Krivovichev, V.G., Linthout, K., LAIRD, J., MARESCH, W.V., SCHUMACHER, J.C., STEPHENSON, N.C., WHITTAKER, E.J., 1997. Nomenclature of amphiboles: report of the subcommittee on amphiboles of the International Mineralogical Association, Commission on New Minerals and Mineral Names. Can Mineral 35, 219246Lindsley.

Ji, S., Wang, Q., Xia, B., 2002. Handbook of seismic properties of minerals, rocks and ores, Presses inter Polytechnique, pp.

Jiang, F., Speziale, S., Duffy, T.S., 2004. Single-crystal elasticity of grossular-and almandine-rich garnets to 11 GPa by Brillouin scattering. Journal of Geophysical Research: Solid Earth (1978–2012) 109.

Kim, D., Katayama, I., Michibayashi, K., Fabric analyses of experimentally deformed blueschists: Implications for deformational behaviors of sodic amphibole, AGU Fall Meeting Abstracts 1, 2012, p. 2583.

Kim, D., Katayama, I., Michibayashi, K., Tsujimori, T., 2013a. Rheological contrast between glaucophane and lawsonite in naturally deformed blueschist from Diablo Range, California. Island Arc 22, 63-73.

Kim, D., Katayama, I., Michibayashi, K., Tsujimori, T., 2013b. Deformation fabrics of natural blueschists and implications for seismic anisotropy in subducting oceanic crust. Physics of the Earth and Planetary Interiors 222, 8-21.

Knowles, C.R., 1987. A BASIC program to recast garnet end members. Computers & Geosciences 13, 655-658.

Krogh, E., Oh, C., Liou, J., 1994. Polyphase and anticlockwise P-T evolution for Franciscan eclogites and blueschists from Jenner, California, USA. Journal of Metamorphic Geology 12, 121-134.

Long, M.D., van der Hilst, R.D., 2005. Upper mantle anisotropy beneath Japan from shear wave splitting. Physics of the Earth and Planetary Interiors 151, 206-222.

Long, M.D., van der Hilst, R.D., 2006. Shear wave splitting from local events beneath the Ryukyu arc: trench-parallel anisotropy in the mantle wedge. Physics of the earth and planetary interiors 155, 300-312.

Mainprice, D., 1990. A FORTRAN program to calculate seismic anisotropy from the lattice preferred orientation of minerals. Computers & Geosciences 16, 385-393.

Mao, Z., Jiang, F., Duffy, T.S., 2007. Single-crystal elasticity of zoisite Ca2Al3Si3O12 (OH) by Brillouin scattering. American Mineralogist 92, 570-576.

Mauler, A., Godard, G., Kunze, K., 2001. Crystallographic fabrics of omphacite, rutile and quartz in Vendée eclogites (Armorican Massif, France). Consequences for deformation mechanisms and regimes. Tectonophysics 342, 81-112.

Nakajima, J., Hasegawa, A., 2004. Shear-wave polarization anisotropy and subduction-induced flow in the mantle wedge of northeastern Japan. Earth and Planetary Science Letters 225, 365-377.

Nakajima, J., Shimizu, J., Hori, S., Hasegawa, A., 2006. Shear-wave splitting beneath the southwestern Kurile arc and northeastern Japan arc: A new insight into mantle return flow. Geophysical research letters 33.

Oh, C.-W., Liou, J., 1990. Metamorphic evolution of two different eclogites in the Franciscan Complex, California, USA. Lithos 25, 41-53.

Panozzo, R., 1984. Two-dimensional strain from the orientation of lines in a

plane. Journal of Structural Geology 6, 215-221.

Pera, E., Mainprice, D., Burlini, L., 2003. Anisotropic seismic properties of the upper mantle beneath the Torre Alfina area (Northern Apennines, Central Italy). Tectonophysics 370, 11-30.

Piepenbreier, D., Stöckhert, B., 2001. Plastic flow of omphacite in eclogites at temperatures below 500 C–implications for interplate coupling in subduction zones. International Journal of Earth Sciences 90, 197-210.

Polet, J., Kanamori, H., 2002. Anisotropy beneath California: shear wave splitting measurements using a dense broadband array. Geophysical Journal International 149, 313-327.

Pozgay, S.H., Wiens, D.A., Conder, J.A., Shiobara, H., Sugioka, H., 2007. Complex mantle flow in the Mariana subduction system: evidence from shear wave splitting. Geophysical Journal International 170, 371-386.

Raymond, L.A., Bero, D.A., 2015. Sandstone-matrix mélanges, architectural subdivision, and geologic history of accretionary complexes: A sedimentological and structural perspective from the Franciscan Complex of Sonoma and Marin counties, California, USA. Geosphere 11, 1077-1110.

Rickwood, P., 1968. On recasting analyses of garnet into end-member molecules. Contributions to mineralogy and petrology 18, 175-198.

Ross, J., Sharp, W., 1986. 40Ar/39Ar and Sm. Nd dating of garnet amphibolite in the Coast Ranges, California: Eos (Transactions, American Geophysical Union) 67, 1249.

Ross, J., Sharp, W., 1988. The effects of sub-blocking temperature metamorphism on the K/Ar systematics of hornblendes: 40Ar/39Ar dating of polymetamorphic garnet amphibolite from the Franciscan Complex, California. Contributions to Mineralogy and Petrology 100, 213-221.

Rudnick, R.L., Fountain, D.M., 1995. Nature and composition of the

continental crust: a lower crustal perspective. REVIEWS OF GEOPHYSICS-RICHMOND VIRGINIA THEN WASHINGTON- 33, 267-267.

Ryzhova, T., Aleksandrov, K., Korobkova, V., 1966. The elastic properties of rock-forming minerals V. Additional data on silicates. Physics of the Solid Earth 2, 63-65.

Schmidt, M.W., Poli, S., 1998. Experimentally based water budgets for dehydrating slabs and consequences for arc magma generation. Earth and Planetary Science Letters 163, 361-379.

Shervais, J.W., Choi, S.H., Sharp, W.D., Ross, J., Zoglman-Schuman, M., Mukasa, S.B., 2011. Serpentinite matrix mélange: Implications of mixed provenance for mélange formation. Geological Society of America Special Papers 480, 1-30.

Skemer, P., Katayama, I., Jiang, Z., Karato, S.-i., 2005. The misorientation index: Development of a new method for calculating the strength of lattice-preferred orientation. Tectonophysics 411, 157-167.

Teyssier, C., Whitney, D.L., Toraman, E., Seaton, N.C., 2010. Lawsonite vorticity and subduction kinematics. Geology 38, 1123-1126.

Tsujimori, T., Matsumoto, K., Wakabayashi, J., Liou, J., 2006. Franciscan eclogite revisited: Reevaluation of the P–T evolution of tectonic blocks from Tiburon Peninsula, California, USA. Mineralogy and Petrology 88, 243-267.

Vaughan, M.T., Guggenheim, S., 1986. Elasticity of muscovite and its relationship to crystal structure. Journal of Geophysical Research: Solid Earth (1978–2012) 91, 4657-4664.

Wakabayashi, J., 1990. Counterclockwise PTt paths from amphibolites, Franciscan Complex, California: Relics from the early stages of subduction zone metamorphism. The Journal of Geology, 657-680.

Wakabayashi, J., 1992. Nappes, tectonics of oblique plate convergence, and metamorphic evolution related to 140 million years of continuous

subduction, Franciscan Complex, California. The Journal of Geology, 19-40.

Wakabayashi, J., 2015. Anatomy of a subduction complex: architecture of the Franciscan Complex, California, at multiple length and time scales. International Geology Review 57, 669-746.

Wakabayashi, J., Dumitru, T.A., 2007. 40Ar/39Ar ages from coherent, high-pressure metamorphic rocks of the Franciscan Complex, California: revisiting the timing of metamorphism of the world's type subduction complex. International Geology Review 49, 873-906.

Zhang, J., Green, H.W., Bozhilov, K.N., 2006. Rheology of omphacite at high temperature and pressure and significance of its lattice preferred orientations. Earth and Planetary Science Letters 246, 432-443.

List of Tables

List of Figures

lineation, N: number of grains, and M: M-index of LPO.

Figure 6. LPOs of epidote. They are plotted in the lower hemisphere using an equal area projection (half scatter width = 20˚). S: foliation, L: lineation, N: number of grains, and M: M-index of LPO.

Figure 7. LPOs of phengite. They are plotted in the lower hemisphere using an equal area projection (half scatter width = 20˚). S: foliation, L: lineation, N: number of grains, and M: M-index of LPO.

Figure 8. LPOs of garnet. They are plotted in the lower hemisphere using an equal area projection (half scatter width = 20˚). S: foliation, L: lineation, N: number of grains

Figure 9. Seismic anisotropy and velocity of glaucophane. E-W direction: lineation, center of a stereographic projection: normal to foliation.

Figure 10. Seismic anisotropy and velocity of omphacite. E-W direction: lineation, center of a stereographic projection: normal to foliation.

Figure 11. Seismic anisotropy and velocity of epidote. E-W direction: lineation, center of a stereographic projection: normal to foliation.

Figure 12. Seismic anisotropy and velocity of phengite. E-W direction: lineation, center of a stereographic projection: normal to foliation.

Figure 13. Seismic anisotropy and velocity of garnet. E-W direction: lineation, center of a stereographic projection: normal to foliation.

Figure 14. Seismic anisotropy and velocity of whole rocks. E-W direction: lineation, center of a stereographic projection: normal to foliation.

Figure 15. Effect of dip angle (θ) on the seismic anisotropy of minerals and whole rock in sample 2425. The X and Z directions indicate the lineation and the normal to foliation direction, respectively. **A**. glaucophane, **B**. phengite, **C**. whole rock

Figure 16. Effect of dip angle (θ) on the seismic anisotropy of glaucophane, phengite and whole rock of sample 2425. (A) horizontal flow, (B) flow dipping at 30°, (C) flow dipping at 45°, (D) flow dipping at 60°, (E) flow dipping at 70°. The X and Z directions indicate the lineation and the normal to foliation direction, respectively.

국문 초록

대부분의 섭입대에서 비교적 강한 지진파 비등방성이 관찰되고 있다. 섭입대에서 해양지각이 맨틀로 섭입하면서 청색편암으로 변성되고, 섭입이 더 진행되어 압력이 높아지면 에클로자이트로 바뀐다. 청색편암은 남섬석 (glaucophane), 로오소나이트, 녹렴석 (epidote), 녹니석 (chlorite)과 같은 여러 함수 광물들로 이루어져 있다. 위의 광물들은 매우 강한 이방성을 보이기 때문에 섭입대의 지진파 속도와 비등방성은 이들의 격자선호방향에 기인할 수 있다. 그러므로 청색편암의 미구조에 관한 연구는 섭입하는 해양지각의 지진파 특성들을 이해하는 데 중요하다.

본 연구에서는 캘리포니아의 링 마운틴과 제너에서 산출되는 청색편암과 에클로자이트의 미구조와 지진파 특성들을 조사하였다. 청색편암 샘플들은 주로 남섬석, 녹렴석, 펜자이트 (phengite)로 이루어져 있으며 에클로자이트는 녹휘석 (omphacite), 각섬석, 녹렴석, 석류석으로 이루어져 있다. 본 연구에서는 서울대학교 지구환경과학부에 있는 SEM/EBSD 를 사용하여 주요 구성 광물들의 격자선호방향을 결정하였다. 그리고 지진파 비등방성은 각 광물들의 격자선호방향, 밀도, 탄성 상수 (C_{ij})를 이용하여 계산하였다.

청색편암의 구성 광물 중 가장 큰 비율을 차지하는 남섬석은 다른 광물들과는 다르게 링 마운틴과 제너에서 격자선호방향이 각각 다르게 나타났다. [001] 축의 경우 링 마운틴 샘플에서는 선구조에 거의 평행하게

배열하고, 제너 샘플에서는 엽리면에 거의 평행한 거들을 보였다. 이외의 축과 면들에서는 패턴은 유사하였으나 제너 샘플들은 비교적 약한 격자 선호 방향성을 보였다. 지진파 비등방성은 Ring Mt.에서 더 크게 나타났다. 녹렴석은 두 지역의 샘플 모두 [001]축과 (110), (010)면이 선구조와 거의 수직하게 배열하였고 지진파 비등방성은 남섬석보다 작았다. 일부 청색편암 샘플들에서는 펜자이트가 많이 관찰되는데, 이 광물은 [001]축과 (110), (010) 면이 엽리면에 거의 수직하고, [100]축이 엽리면에 평행한 격자 선호 방향을 보였다. 또한 다른 광물들에 비해 아주 큰 지진파 비등방성을 보였다. 에클로자이트의 녹휘석은 [001]축이 선구조와 아평행하고 (010)면이 엽리에 아평행하게 배열된 방향성을 보였다. 녹휘석의 지진파 비등방성은 계산된 주요 구성 광물들 중에서 가장 작게 나타났다. 각 광물들의 지진파 비등방성과 구성 비율을 고려하여 전체 암석의 지진파 비등방성을 계산하였다. 같은 광물 조합을 보이는 샘플들끼리 비교해보면 링 마운틴의 샘플들이 제너의 샘플들보다 더 큰 지진파 비등방성을 보였다. 특히 펜자이트를 많이 포함하고 있는 청색편암은 아주 큰 지진파 비등방성을 보였다 (AV_P = 30 %, max.AV_S = 23 %). 또한 에클로자이트는 녹휘석의 영향으로 지진파 비등방성이 청색편암보다 현저히 작게 나타났다 (청색편암: AV_P = 12−30%, max.AV_S = 9−23%, 에클로자이트: AV_P = 5−6%, max.AV_S = 4−6%). 따라서 청색편암이 섭입대에서 관찰되는 강한 지진파 비등방성에 더 큰 기여를 할 수 있을 것으로 보인다.

주요어: 청색편암, 에클로자이트, 펜자이트, 격자 선호 방향, 지진파 비등방성, 프란시스칸 콤플렉스

학번: 2014-20322